THESIS FOR THE DEGREE OF DOCTOR OF PHILOSOPHY IN MACHINE AND VEHICLE SYSTEMS

Wheel Modelling and Cooling Flow Effects on Car Aerodynamics

TEDDY HOBEIKA

Department of Mechanics and Maritime Sciences

Division of Vehicle Engineering and Autonomous Systems

CHALMERS UNIVERSITY OF TECHNOLOGY

Gothenburg, Sweden 2018

Wheel Modelling and Cooling Flow Effects on Car Aerodynamics
TEDDY HOBEIKA
ISBN 978-91-7597-687-7

Doktorsavhandlingar vid Chalmers tekniska högskola
Ny serie nr. 4368
ISSN 0346-718X
Department of Mechanics and Maritime Sciences
Division of Vehicle Engineering and Autonomous Systems
Chalmers University of Technology
SE-412 96 Gothenburg
Sweden
Telephone: +46 (0)31-772 1000

Chalmers Reproservice
Gothenburg, Sweden 2018

Wheel Modelling and Cooling Flow Effects on Car Aerodynamics
Thesis for the degree of Doctor of Philosophy in Machine and Vehicle Systems
TEDDY HOBEIKA
Department of Mechanics and Maritime Sciences
Division of Vehicle Engineering and Autonomous Systems
Chalmers University of Technology

Abstract

In recent years, the automotive industry has focused on computer simulations as an alternative to physical testing. This allows for early vehicle optimization, short turn around times, and significant cost savings. Aerodynamics is an important vehicle attribute where Computational Fluid Dynamics (CFD) simulations are being used to improve vehicle design. In this context, predicting the aerodynamic forces in CFD is challenging, given the complexity of both the geometry and the flow. Two main areas where discrepancies between CFD and wind tunnel tests are present are wheel aerodynamics and cooling flow.

Wheel aerodynamics has been the focus of CFD research for several years, especially with the expected introduction of the Worldwide harmonized Light vehicles Test Procedure (WLTP) regulations. Car manufactures will need to evaluate the drag of the vehicle for all different rim and tyre combinations sold with the car, in order to determine its official fuel consumption. Thus, accurate modelling of tyre and rims in CFD is a high priority for vehicle manufacturers, in order to optimize vehicle design without large increases in testing costs. This thesis investigates the effects of different wheel geometries, as well as different wheel rotation modelling techniques and their effect on overall vehicle forces. A hybrid approach for modelling tyre rotation, named MRFg, has been proposed and analysed. It showed significant improvements in numerical prediction, when compared to experimental results. MRFg can be applied on the loaded and deformed tyres with no significant cost increase. Investigations into the tyre geometry also showed that the CFD accuracy can be improved by reproducing the rain grooves' continuity at the contact patch in the virtual model. The rain grooves have been show to reduce overall vehicle drag in both the wind tunnel tests and the simulations.

The cooling flow is an important parameter to consider when validating simulations to experiments, as it changes the flow field around the vehicle and has a large impact on the aerodynamic forces. In this thesis, a simple and quick method for measuring cooling flow is introduced. It is a force based approach where the force acting on the radiator core is used to calculate the air mass flow. It allows for non-intrusive monitoring of the cooling flow and forces during aerodynamic development with good accuracy. A comparison of CFD and wind tunnel tests is also performed with focus on parameters influencing cooling flow and force measurements. The effects of wind tunnel blockage and measurement grid have been shown to have significant effects on mass flow predictions.

Keywords: CFD, Aerodynamics, wheels, tyres, cooling flow, cooling drag, rotation modelling

Acknowledgements

I would like to thank Dr. Christoffer Landström, Dr. David Söderblom, and Dr. Peter Gullberg for their guidance, support, and enlightening discussions.

A big thanks to Prof. Simone Sebben, my main supervisor, for her constant guidance throughout my PhD project and without whom this project would not have been possible.

I would also like to thank Prof. Lennart Löfdahl, my examiner, who has opened doors to numerous opportunities.

I would also like to thank Volvo Cars for providing access to their wind tunnel as well as providing access to their clusters for performing simulations.

A big thanks to my steering committee and the Swedish Energy Agency for providing funding and support for my PhD project.

Some of the simulations were performed on resources provided by the Swedish National Infrastructure for Computing (SNIC) at PDC Center for High Performance Computing (PDC-HPC)

Last by not least, A big thank you for my colleagues and ex-colleagues, not limited to the second floor, for all the very interesting heated discussions/arguments, laughs, and coffee breaks.

Abbreviations

Symbol	Definition
CFD	Computational Fluid Dynamics
WT	Wind tunnel
WLTP	Worldwide harmonized Light vehicles Test Procedure
WLTC	Worldwide harmonized Light vehicles Test Cycle
NEDC	New European Driving Cycle
IDDES	Improved Delayed Detached Eddy Simulation
RW	Rotation Wall
MRF	Moving Reference Frame
MRFg	Moving Reference Frame - grooves
SM	Sliding Mesh
CFL	Courant Friedrichs Lewy
CAD	Computer Aided Design
S	Slick tyre
R	Rain grooved tyre
G	Lateral grooved tyre
D	Detailed tyre
CR	Closed Rim
OR	Open Rim

Nomenclature

Symbol	Definition	Units
C_d	Drag Coefficient	-
C_l	Lift Coefficient	-
F_{drive}	Driving force	N
m	Mass	kg
a	Acceleration	m/s^2
α	Road inclination *deg*	
g	gravity	m/s^2
μ_{road}	Road-tyre friction coeffcient	-
$A_{frontal}$	Car frontal area	m^2
ρ	Fluid density	kg/m^3
V	Test velocity	m/s
$\vec{u_p}$	Relative velocity	m/s
$\vec{u_0}$	Absolute velocity	m/s
$\vec{\omega_p}$	Angular velocity	rad/s
p	Fluid pressure	Pa
v_{avg_core}	Average velocity through radiator	m/s
$\dot{m}_{core}$	Mass flow through radiator	kg/s
$\dot{V}_{core}$	Volumetric flow through radiator	m^3/s
ρ_{air}	Air density	kg/m^3
A_{core}	Area of Radiator Core	m^2

Thesis

This thesis consists of an extended summary and the following appended papers:

Paper A T. Hobeika, S. Sebben, and C. Landstrom. Investigation of the Influence of Tyre Geometry on the Aerodynamics of Passenger Cars. *SAE International Journal of Passenger Cars - Mechanical Systems* 6 (1 2013), pp. 316–325. ISSN: 1946-4002. DOI: 10.4271/2013-01-0955

Paper B T. Hobeika, S. Sebben, and L. Lofdahl. "Study of Different Tyre Simulation Methods and Effects on Passenger Car Aerodynamics". *International Vehicle Aerodynamics Conference 2014*. Holywell Park, Loughborough, UK, 2014, pp. 187–195. ISBN: 978-0-08-100199-8

Paper C T. Hobeika, S. Sebben, and L. Löfdahl. Experimental and numerical investigations of cooling drag. *Proceedings of the Institution of Mechanical Engineers, Part D: Journal of Automobile Engineering* 231.9 (2017), pp. 1203–1210. DOI: 10.1177/0954407016684740

Paper D T. Hobeika et al. Force Based Measurement Method for Cooling Flow Quantification. *SAE International Journal of Passenger Cars - Mechanical Systems* 10.2 (Mar. 2017), pp. 619–627. ISSN: 1946-4002. DOI: 10.4271/2017-01-1520

Paper E T. Hobeika and S. Sebben. CFD Investigation on Wheel Rotation Modelling. *Journal of Wind Engineering and Industrial Aerodynamics* 174 (2018), pp. 241–251. ISSN: 0167-6105

Paper F T. Hobeika and S. Sebben. "Tyre Pattern Features and their Effects on Passenger Vehicle Drag". *Accepted for publication in conjunction with SAE 2018 World Congress & Exhibition. Paper no: 2018-01-0710*

Division of Work

All simulations presented in the above publications are set up, performed, and analysed by Hobeika. Except for Paper A, all wind tunnel tests are also designed, supervised, and analysed by Hobeika.

The wind tunnel results presented in Paper A are obtained from Landström. The calibration test performed in Paper D has been performed under the supervision and guidance of Gullberg.

Contents

Part I
Extended Summary

Chapter 1

Introduction

1.1 Environment and Regulations

During recent decades, environmental concerns regarding global warming have been raised worldwide. It is clear that the planet is changing in ways humans could not have predicted. This phenomena is widely known as climate change and shows itself in various ways: the rise in global surface temperatures, thinning of the Ozone layer, shrinking of the polar ice caps, etc. All of which are strongly dependent on the steep rise in green house gasses concentration in the atmosphere. These gasses enhance the planet's heat retaining capability. CO_2 gas is a major green house agent which has been massively released into the atmosphere due to human activity and industrial developments in the past century. CO_2 emissions in Europe in 2014, from various sectors, is presented in Figure 1.1.

Transport is a major contributor of CO_2 emissions covering around 18 % of the overall emissions. Transportation vehicles are generally operated by combustion of various types of fuels, which releases numerous emissions. CO_2 is among the biggest of these emissions for all types of combustion and unlike other gases, or particles, it is not possible to convert it into a less harmful form in add on catalysts or filters. This has led governments around the world to introduce regulations to drive manufacturers to reduce emissions by producing more energy efficient vehicles. Road vehicles have received a large interest in that respect as they are widely spread in cities and populated areas, they also contribute to other forms of pollutions such as soot emissions and smog formation. Figure 1.2 shows the contributions of different types of vehicles to CO_2 emissions, which highlights that road vehicles contribute around 75 % of the overall emissions, in the transportation sector.

This has also led to the introduction of strict regulations by the European Union Council, which aims to bring CO_2 emissions for car fleets down to an average of 95 g/km by 2020

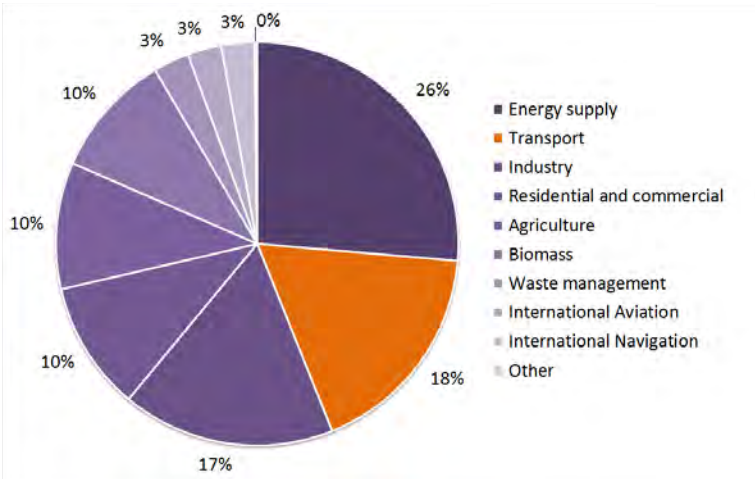

Figure 1.1: *CO_2 emissions in Europe 2014 from different sectors [7].*

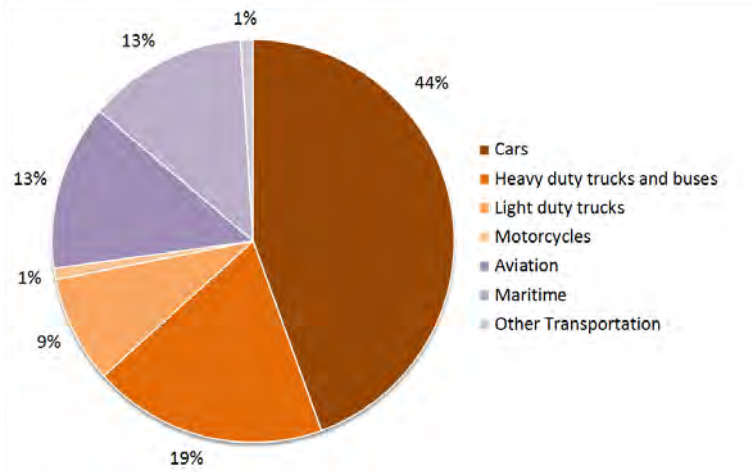

Figure 1.2: *CO_2 emissions in Europe 2014 from different sectors [7].*

[8]. Car manufacturers then increased the priority of energy efficiency and have been working hard on reducing all forms of losses and resistances. A closer look at that can be observed by looking at the forces a vehicle needs to overcome when driving,

$$F_{drive} = ma + mgsin(\alpha) + \mu_{road}mg + \tfrac{1}{2}\rho C_d A_{frontal} v^2 \tag{1.1}$$

where F_{drive} is the force that must be produced by the powertrain, m is the mass of the vehicle, a is the desired acceleration, g is gravity, α is the inclination of the road, μ_{road} is the road friction coefficient, ρ is air density, C_d is the drag coefficient, $A_{Frontal}$ is the frontal area of the vehicle, and v is the velocity at which the vehicle is travelling. From

Equation 1.1, and assuming that the vehicle is coasting at a constant speed on a flat road, the resistances are reduced to the rolling resistance, $\mu_{road}mg$, and the aerodynamic resistance, $\frac{1}{2}\rho C_d A_{frontal} v^2$. These resistances are speed dependent and their relation can be seen in Figure 1.3. The aerodynamic resistance becomes more significant than the rolling resistance at speeds above 60 km/h.

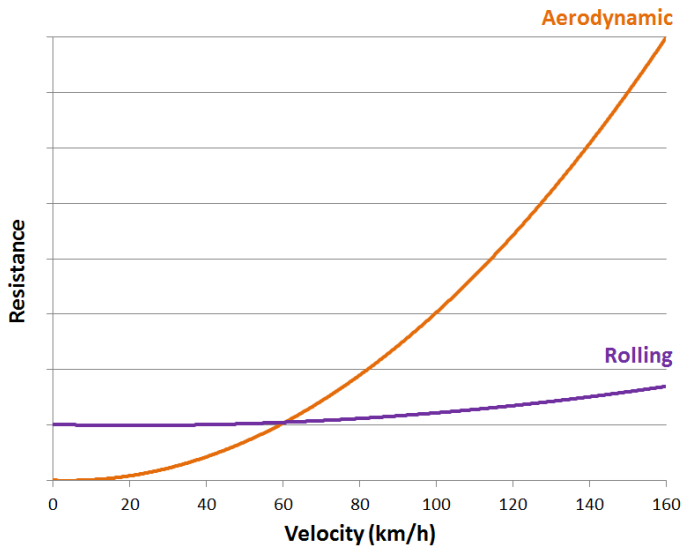

Figure 1.3: *Increase in rolling resistance and aerodynamic resistance with increase in speed.*

Along with setting CO_2 emission levels, The European Council has also set a new testing procedure based on which these emission levels are measured. This procedure is known as the Worldwide harmonized Light vehicles Test Procedure (WLTP) and is gradually being implemented [9]. With the introduction of the WLTP regulations, aerodynamics is given a higher impact as the average speed of the test cycle rises to 46 km/h, compared to the previous, 34 km/h, in the New European Driving Cycle (NEDC). Aerodynamic resistance increases as the vehicle speed increases, and for a passenger car, the aerodynamic resistance typically dominates over 60 km/h. This is visualised in Figure 1.3

The NEDC lasted 20 minutes and consisted of two phases: urban and extra urban. It consists of numerous constant accelerations to a certain speed, which is maintained for a certain time, followed by a constant deceleration. There are stops in between these different cycles where the engine is idling. The total idle time adds up to 27 % of the total cycle duration. The Worldwide harmonized Light vehicles Test Cycle (WLTC) is 10 minutes longer than the NEDC and is split into four phases: low, medium, high, and extra-high. The idling time is reduced to 13 % and the extra-high phase lies mostly above 100 km/h where aerodynamic resistance is almost double the rolling resistance, from Figure 1.3.

The velocity profiles of the test cycles can be seen in Figure 1.4.

Table 1.1: *A short comparison of important parameters between NEDC and WLTC.*

	NEDC	WLTC
Duration (min)	20	30
Idle time (%)	25	13
Cycle Distance (km)	11	23
Driving Speed (km/h)	25	13
Driving phases	2	4
Urban Driving (%)	66	52
Non-Urban Driving (%)	34	48

The increase of the importance of aerodynamics can be seen when comparing the aerodynamic influence on CO_2 emissions, under NEDC and WLTC, on a standard passenger car. In NEDC, improving aerodynamics performance by 5 % reduces CO_2 emissions by around 1.0 g/km. Under WLTC, that would equate to a reduction of around 1.5 g/km, 50 % larger impact than in NEDC. However, the driving cycle is not the only change in WLTP that increases focus on aerodynamics.

1.2 Impact on Wheel Aerodynamics

The validation of the aerodynamic drag of the vehicles, under WLTP, is to be performed for a variety of car configurations and not only a baseline configuration, previously chosen by the vehicle manufacturer. This also includes the various options, tyre and rim configurations for example, that the customer could order on the car. This adds additional challenges for the aerodynamic design of the vehicle since optimizing the vehicle for different tyre and rim configurations through wind tunnel tests becomes quite expensive, as the testing time rises significantly. As an alternative, vehicle manufacturers look at Computational Fluid Dynamics (CFD) simulations to be able to analyse these effects without the need for additional testing time. This is a quite natural move as most of the vehicle design process has been pushed more and more into simulations over the past decade, due to both cost cuts as well as increased accuracy and confidence in simulation results.

1.3 Cooling Flow Optimization

Another area where manufacturers could reduce the overall drag of the vehicles is through the use of active grill shutters, which would vary the grill blockage. Grill shutters are used when the air going through the car's cooling system exceeds the cooling requirements. At this point a grill shutter can be engaged in order to block part of the grill intake and limit the airflow through the engine bay, thus reducing cooling flow and reducing the vehicle's overall drag. Optimization of such a system does not vary a lot from the normal

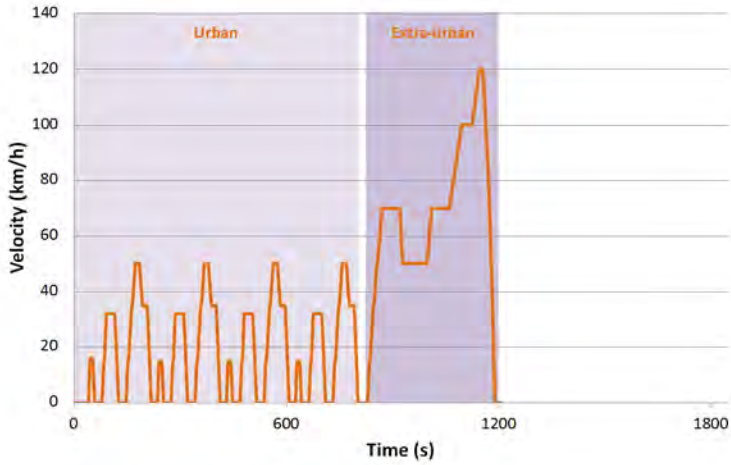

(a) *Non-circular form*

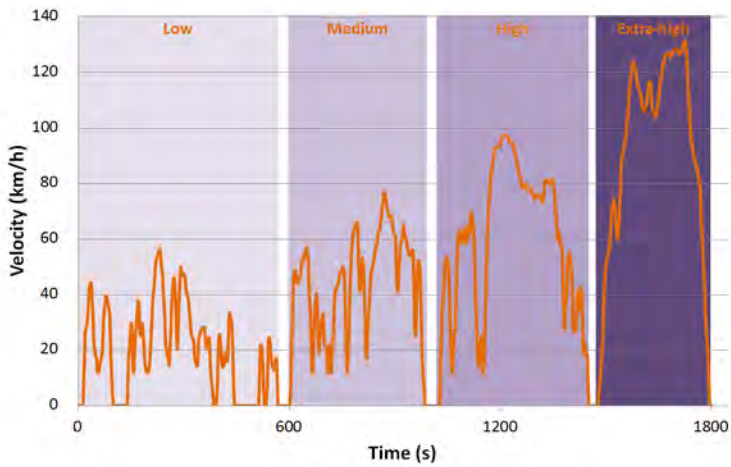

(b) *WLTC*

Figure 1.4: *Velocity profiles of the test cycles.*

optimization routines for cooling flow, where knowledge of the mass flow through the radiator is desirable. With a general push in industry to increase system efficiencies and push optimization limits, the need for fast, accurate, and cheap methods increases.

1.4 Project Objectives

This project aims at improving the understanding of both wheel aerodynamics and cooling flow. The general objectives can be stated as follows:

- Improving tyre rotation modelling in CFD simulations.
- Investigating tyre geometry effects on overall vehicle force.
- Measuring cooling flow, radiator drag, and overall vehicle drag and lift changes for multiple configurations.
- Comparing cooling flow effects from experiments and simulations.

Chapter 2

Wheel Aerodynamics

2.1 Background Information

Research on tyre and rim designs have been an interesting area for aerodynamicists for a couple decades with papers on wheel aerodynamics dating back to the 70's and increased in popularity during the 90's [10–18], long before the WLTP regulations were drafted. However, one must acknowledge that the research on the topic has been on the rise in recent years and can be seen in [19–33], which focused on rim designs, general wheel aerodynamics, and/or the wheel's interaction with the vehicle. In addition, an increase in research on tyre aerodynamics has been clear [34–42], with focus on the tyre geometry, tyre modelling techniques, and the tyre's aerodynamic effect on the rest of the vehicle.

Pressure measurements performed on the centre line of a rotating isolated road wheel have been performed by Fackarell and Harvey [10]. In the observations, the pressure coefficient (C_p) rises above one at the contact patch with rotating wheels. This has been explained by a wheel jetting effect where the wheel rotation applies work to the flow. This has been also measured later by Mears, Dominy, and Sims-Williams [19] where a similar peak in pressure to around $C_p = 2$ has been observed. Yet, with rain grooves added to the tyres, the C_p at the contact patch has been observed to remain below 1. This has been explained by the suppression of the wheel jetting by the rain grooves. More importantly a negative pressure peak can be observed downstream of the contact patch with values up to -1.5 in C_p [19, 20]. These changes in pressure have large effects on the flow around the wheel and thus highlight the importance of preserving tyre grooves at the ground when performing CFD simulations.

However, preserving the tyre pattern at the contact patch is not the only challenge for modelling tyre rotation in CFD. The tyre is not a rigid body, and while it rotates it undergoes deformations due to centrifugal forces, namely radial expansion and axial

contraction shown by Landstrom et al. [37]. If the car is equipped with a suspension which allows for wheel movement, the wheel centre will also lift up into the wheel house as also shown by Landstrom et al. [37]. Sprot, Sims-Williams, and Dominy [42] also showed that as the tyre lifting, inflation pressures, and vertical loading, affect the bulging at the contact patch and the tyre profile. This can significantly alter the flow around an exposed wheel. Experimental investigations into certain features of the tyre that influence separation have been investigated by Wittmeier et al. [35] in both model scale and full scale tests. From the various configurations it could be seen that smooth tyre profiles and side walls are important to achieve low drag values. These effects matched well between in both model and full scale tests. Investigations on the changes in tyre width and tyre pattern have been performed by Mercker et al. [13]. They showed significant variations in drag when varying the tyre width and pattern separately. In Mercker et al. [13], the slick tyre showed the lowest drag value. However, when slicks are tested against detailed tyres on a closed rim by Wickern, Zwicker, and Pfadenhauer [18], the detailed tyres resulted in the lower drag. This sheds some light on the complexity of tyre aerodynamics and its interaction with the rims.

The tyre geometry alone is very challenging to match with experiments, and modelling the rotation adds more difficulty to the problem at hand. The tyre involves complex pattern details, it bulges at the ground under vehicle load, and it looses its circular form at the contact patch, all of which can be seen in Figure 2.1. This makes if problematic to mesh the fine pattern details, take deformation into account, and apply representative boundary conditions.

In the majority of CFD simulations, the tyres are represented as slicks and sometimes they are kept completely undeformed and are simply cut off at the contact patch. However different, approaches to modelling tyre rotation have been investigated. One approach is to take a slick deformed representation of the tyre and apply numerical surface roughness [36]. Yet, the surface roughness values need to be tuned for every tyre, with different surface roughness used for different parts of the tyre. Other approaches looked into keeping the full tyre pattern and circular form, no deformation, while using an Immersed Boundary approach to move the tyre mesh every time step [43]. Yet, since the tyre is left undeformed, this leads to an incorrect wheel centre position and/or an oversized contact patch area.

This work presents an alternative approach, named MRFg, where the tyre is deformed and the major features of the tyre could be kept and modelled.

2.2 Rotation Modelling Methods

In CFD, rotation can be modelled in various ways and to each its advantages and disadvantages. Three basic rotation modelling approaches are described in this section: The Rotating Wall (RW), Moving Reference Frame (MRF), and the Sliding Mesh (SM). This is followed by the hybrid approach, Moving Reference Frame - grooves (MRFg) proposed in this thesis for tyre rotation modelling.

(a) *Side bulge*

(b) *Non-circular form*

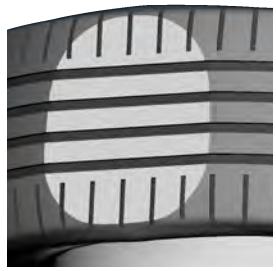

(c) *Contact patch*

Figure 2.1: *Tyre deformation under vehicle load.*

2.2.1 Rotating Wall

The Rotating Wall approach is implemented by setting a rotational velocity to the moving boundary. The solver will determine the individual surface cell velocity based on the distance to the axis of rotation and angular speed. As this is a solid boundary velocity, it can only be applied tangential to the wall. Hence, if the velocity vector does not lie in the same plane as the surface cell, it is typically projected, thus loosing its normal component.

For this reason, the Rotating Wall boundary condition is not feasible when the desired velocity implementation is normal to the cell surface. This is typically the case on the rim spokes and lateral grooves. Figure 2.2 shows the wheel surface velocities resulting from a RW implementation, Figure 2.2a compared to the desired velocity, Figure 2.2b obtained through Sliding Mesh, in this case.

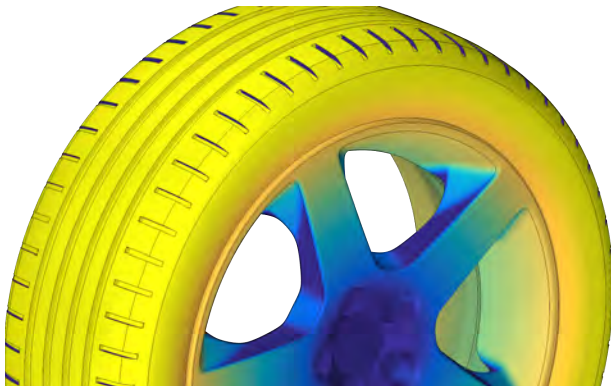

(a) *Rotating wall*

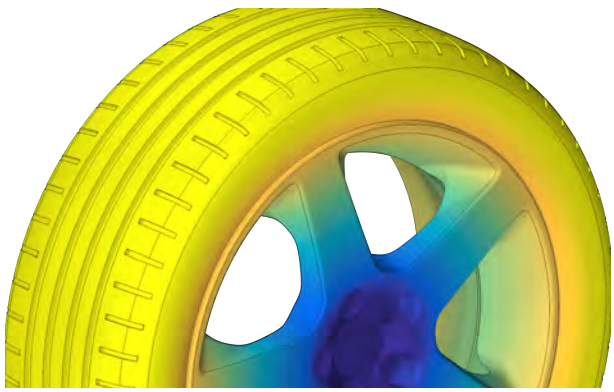

(b) *Sliding Mesh*

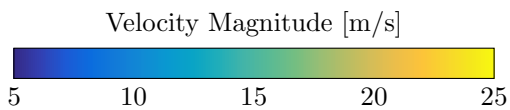

Figure 2.2: *Velocity distribution on a wheel obtained through Rotating Wall (a) vs. Desired velocity obtained through Sliding Mesh(b).*

2.2.2 Moving Reference Frame

The Moving Reference Frame approach is implemented by prescribing the fluid cells, or regions, to a rotating reference frame. This allows it to apply a surface velocity normal to the surface. Hence the MRF approach can produce the desired surface velocity if the complete wheel is part of the MRF region. It also introduces the centrifugal accelerations and Coriolis effects into the fluid.

However, MRF cannot identify which cells in the MRF region are affected by the rotation and which ones are not. It is the CFD user who determines the size of the MRF region

around the rotating object, and the Navier-Stokes equations are modified accordingly in all region cells. From the Star-CCM+ user guide, the Navier-Stokes equations in the moving frame with absolute velocity formulation are as follows:

$$\nabla \cdot (\vec{u_p} \otimes \vec{u_0}) + \vec{\omega_p} \times \vec{u_0} = -\nabla(p/\rho) + \nu \nabla \cdot \nabla \vec{u_0} \tag{2.1}$$

$$\nabla \cdot \vec{u_0} = 0 \tag{2.2}$$

where $\vec{u_p}$ is the velocity relative to the moving reference frame, $\vec{u_0}$ is the absolute velocity, $\vec{\omega_p}$ is the angular velocity of the rotating frame, p is the fluid pressure, and ρ is the fluid density.

If an empty MRF region were to be prescribed in a uniform flow field, then $\nabla \vec{u_0} = 0$. Equation 2.1 can be simplified to

$$\nabla p = -\rho(\vec{\omega_p} \times \vec{u_0})$$

Hence, whenever $\vec{\omega_p} \times \vec{u_0} \neq 0$, a pressure gradient is introduced even if there are no rotating boundaries affecting the flow. A special case where ∇p becomes zero, is when the flow is along the axis of rotation, as for example for an axial fan operating in the high mass flow range. However for wheels, the flow is extremely complex, and the axis of rotation is almost orthogonal to the oncoming flow.

A simple illustration of the problem can be performed in 2D by creating an empty MRF circular region, as large as a wheel, rotating around an axis orthogonal to the fluid domain. Figure 2.3a shows the results when MRF is applied to the circular region versus when Sliding Mesh is applied, Figure 2.3b. It can be seen that the pressure gradient alters the flow field significantly. The velocity changes at the extremities of the fluid zone reach 40 % change to the free stream velocity. Since the velocity is affected, then $\vec{u_0}$ is not equal to zero, as initially assumed, and the simulation shows that ∇p converges to $-\frac{1}{2}\rho(\vec{\omega_p} \times \vec{u_0})$.

2.2.3 Sliding Mesh

The Sliding Mesh approach is implemented by physically moving the mesh each time step. Naturally, this would require an unsteady simulation setup and a separate region. This would be the most realistic way of modelling rotating rigid geometry. The connection between the sliding and stationary region, the interface, needs to be updated every time step as well. This motion, allows SM to take into account the different positions of the rotating object. However, it would typically result in significant increase in simulation time. Rims introduce strong rotation into the flow and their modelling is important for accurate prediction of vehicle drag. For that reason the Sliding Mesh approach is the method of choice when investigating wheels [31–33, 44, 45].

From Figure 2.2b, it can be seen that SM is able to produce the desired velocity distribution on the surface of the wheel. It is also able to preserve uniform flow field even with the

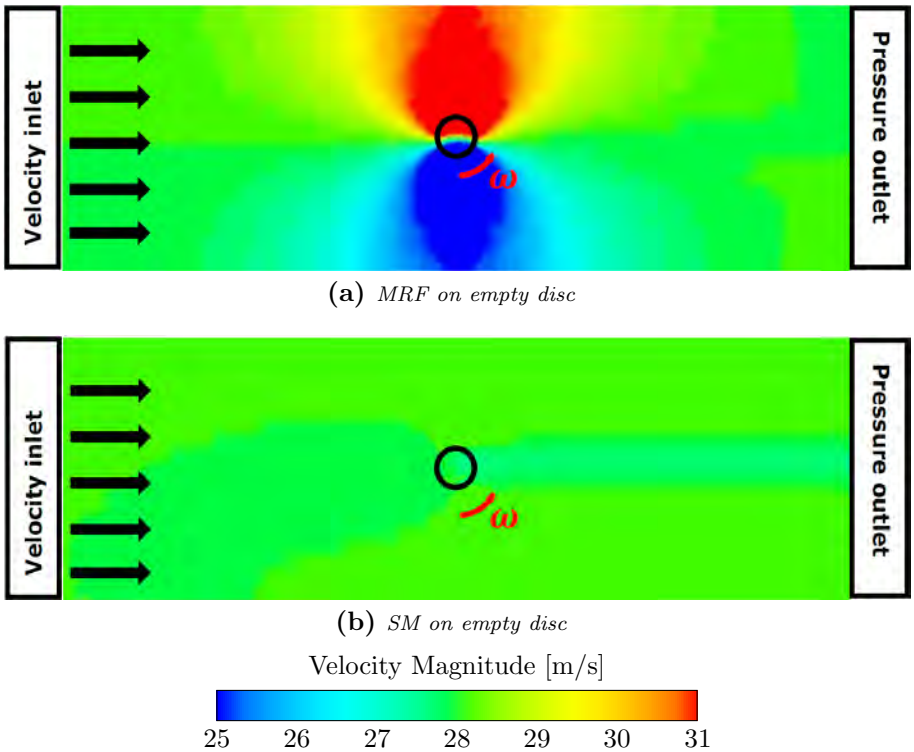

(a) *MRF on empty disc*

(b) *SM on empty disc*

Figure 2.3: *Velocity distribution in a fluid clip plane where two different methods are used to apply rotation on an empty cylindrical volume in a uniform flow field*

mesh motion as shown in Figure 2.3b. For that purpose, SM is used as reference for comparing the various modelling approaches.

2.2.4 Moving Reference Frame - grooves

The Moving Reference Frame - grooves approach is a hybrid between Rotating Wall and MRF. It addresses the weaknesses of RW by applying an MRF in the regions where RW is not adequate. The MRFg approach does not include any mesh motion so it does not take into account the various geometry positions. However, for a geometry with a high order of rotational symmetry or a highly repetitive pattern, such as tyres, it might not be necessary to take the various tyre positions into consideration. So in an MRFg application on tyres, the lateral grooves volumes would be placed in MRF regions. Although the flow in these grooves is not along the axis of rotation, they are under strong rotation effects. A summary of the differences between the various modelling methods is presented in Table 2.1.

Table 2.1: *A short summary of various aspects of the different modelling methods .*

	SM	**MRF**	**RW**	**MRFg**
Applied on	Region	Region	Boundary	Boundary & Region
Steady State	No	Yes	Yes	Yes
Unsteady	Yes	Yes	Yes	Yes
Increases simulation time	Yes	No	No	No
Mesh motion	Yes	No	No	No
Requires circular region	Yes	No	No	No

The MRFg approach had been first introduced in [2]. It was an initial attempt to observe possible effects introduced by the method when only correcting for the surface velocity within the lateral grooves. For this reason, it has been applied on only the first cell on the boundary surface. The MRF region is highlighted in red in Figure 2.4.

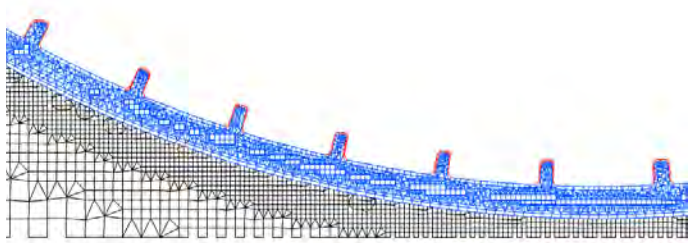

Figure 2.4: *Mesh clip plane through the lateral grooves. The MRF region in the first MRFg investigation is coloured in red.*

At a later stage, a more thorough investigation has been performed which relied on an isolated wheel setup. The setup resulted in a larger MRF region that fills up the lateral groove which allows for a more practical implementation of MRFg, the new MRF region can be seen in grey in Figure 2.5.

Figure 2.5: *The MRF region, coloured in grey, in the improved MRFg method.*

2.3 Experimental Setup

All full vehicle experiments are performed at the Volvo Cars Aerodynamic Wind Tunnel (PVT) at a test speed of 100 km/h. The closed loop tunnel has a slotted wall test section with a cross sectional area of 27 m^2. The tunnel is equipped with a boundary layer control system (BLCS) to reproduce road conditions. The BLCS includes a five belt moving ground system, two distributed suction zones located upstream of the vehicle, and a floor boundary scoop at the beginning of the test section.

The test vehicle is mounted in a fixed position on four support struts. The struts and wheel drive units, are all connected to a Pfister six component balance under the test section. The force measurements, obtained from the balance, are then transformed to dimensionless aerodynamic coefficients. The force resisting the forward motion of the vehicle, the drag force, is used to calculate the drag coefficient (C_d) by

$$C_d = F/\tfrac{1}{2}\rho A_{frontal} V^2 \tag{2.3}$$

where F is the measured force, ρ is the air density, $A_{frontal}$ is the frontal area of the car, and V is the testing speed. The air density is calculated from temperature, humidity, and barometric pressure measurements performed by the wind tunnel system for each measurement throughout testing. Finally, corrections for solid blockage, wake blockage, and horizontal buoyancy are performed in order to obtain a corrected C_d. The final corrected C_d is independent of air density and blockage, hence directly comparable to the simulated C_d in open road conditions. The tunnel has a repeatability uncertainty in C_d measurements of 0.001 within the same test and the measurement and correction process is accredited according to the European Accreditation procedure EA 4/02 [46].

2.4 Vehicle and Tyre Geometry

The test vehicle is a production Volvo S 60 with a rigid suspension. This special chassis enables the control of the wheel centres and trim heights separately. It also fixes the wheel centres in one controlled position throughout testing. The vehicle has a detailed engine bay and cooling package and the cooling inlets were kept open in Paper A. However for papers E and F, the cooling inlets have been blocked by a stiff aluminium plate. Also, numerous split lines across the vehicle have been taped.

In order to produce a comparable vehicle model, a fully detailed S 60 CAD model has been adjusted to fit the physical geometry. All of the above modifications have been replicated including the rigid suspension geometry, inlet closing, and split line taping. The trim heights and wheel centres are also adjusted. The test vehicle and its numerical representation can be seen in Figure 2.6.

The tyres used in Papers E and F are modified racing tyres from Avon. They are initially four sets of slick tyres (210/635R17), 640 mm in diameter and 218 mm wide. Three of the sets have been cut in order to produce a rain grooved set (R), a lateral grooved set (G), and detailed set (D). The four tyre treads can be seen in Figure 2.7.

The tyre profile and geometry is obtained by 3D scanning it while mounted on the testing rims and inflated to the nominal pressure of 1.4 bars. Scanning has also been performed at different tyre pressures going as high as 2.6 bars. When compared, the geometry of the tyre did not change significantly thus showing that the stiff racing tyres are not sensitive to deformation from internal forces. The tyre deformation due to rotation when running at the testing speed of 100 km/h can be neglected. The slick scan has been morphed in order to resemble the loaded tyres in the static position on the car. The pattern details are added to the slick tyres after deformation, so that the tyre contour is identical for all virtual tyre sets.

2.5 Simulation Setup

Three different simulation setups have been used throughout this project with different turbulence modelling methods: a steady state Reynolds Averaged Navier Stokes (RANS), an Unsteady Reynolds Averaged Navier Stokes (URANS), and an Improved Delayed Detached Eddy Simulation (IDDES). The initial steady state setup was a quick tool that allowed for the investigation of numerous configurations during a short period of time. However, in order to allow rim modelling with Sliding Mesh, an unsteady approach had to be adopted. URANS was the closet alternative and enabled the comparison between steady state and unsteady simulations with the same turbulence model, the realizable k-epsilon. At the last stage and for a more accurate comparison to wind tunnel results, the turbulence modelling was changed to the IDDES approach, which is a hybrid RANS-LES model.

(a) *Test vehicle in the wind tunnel*

(b) *Vehicle representation in the numerical domain*

Figure 2.6: *Illustration of the vehicle in tests and simulations, shown here in the closed cooling configuration with open rims.*

2.5.1 Steady State RANS

The steady state RANS setup utilized the realizable k-epsilon for turbulence modelling and was performed in FLUENT (v12). The near wall treatment used is the standard wall function and the y^+ values were between 30 and 100 for the majority of the cells. The coupled pressure-velocity flow solver was used with 2^{nd} order upwind discretization for momentum equations. For gradient computations the Green-Gauss cell based discretization scheme was used.

The simulation domain was 50 x 10 x 10 m in order to have no significant blockage effect on the flow around the car. The flow was driven from a uniform 100 km/h velocity inlet

(a) *Slick (S)* **(b)** *Rain grooved (R)* **(c)** *Lateral grooved (G)* **(d)** *Detailed (D)*

Figure 2.7: *Investigated tyre sets: physical (top) and virtual (bottom).*

towards a pressure outlet. The ground was set to a moving wall also at 100 km/h while all remaining sides are set to symmetry planes, thus avoiding boundary layer build up on the walls. The vehicle wheels were modelled using Rotating Wall approach, except for the rim spokes which were modelled using MRF. As the vehicle has a detailed under hood with a cooling package, The MRF approach was also used for modelling the cooling fans while the heat exchangers are represented by porous media.

The mesh on the vehicle surface ranged from 1.25 to 5 mm with various refinement boxes in separated regions and around strong flow curvatures, such as the tyres. The mesh sizes ranged between 100 to 120 million cells and some mesh planes, showing the mesh distribution, were presented in Figure 2.8.

2.5.2 URANS

The URANS simulations, performed in FLUENT (v14), enabled Sliding Mesh to be applied while preserving a valid comparison to steady state RANS simulations. Turbulence was modelled using the realizable k-epsilon turbulence model, however the near wall treatment was set to enhanced wall treatment as the y^+ values around the tyres dropped below 30. This was mainly due to the added mesh refinement, down to 0.5 mm inside the tyre pattern. The coupled pressure-velocity flow solver was used with 2^{nd} order upwind discretization for momentum, pressure, and turbulence equations. For gradient computations the Green-Gauss cell based discretization scheme was used. The timestep has been set to $2x10^{-4}$s with six inner iterations, resulting in approximately 1 degree rotation per timestep.

The wind tunnel domain is 50 x 5 x 10 m and only including half of the car. This allowed to reduce simulation cost as the wheels were the main area of interest. The car is raised from the ground so as the tyres are not deformed with a 10 mm gap to the ground. This setup cannot be compared to experimental data as it is not accurate from the physical and geometrical perspectives, however is serves as an indication to the simulation's sensitivity

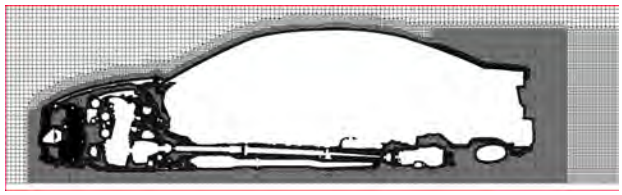

(a) *Mesh clip plane at symmetry plane*

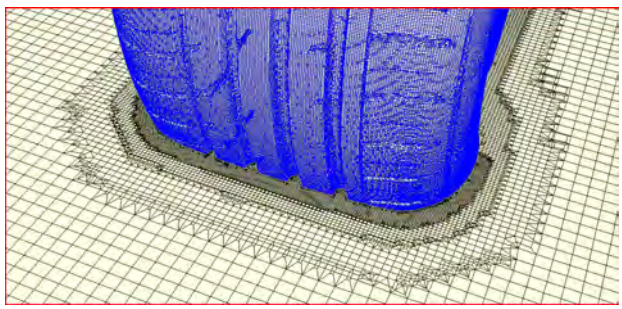

(b) *Mesh clip plane at the tyre also showing surface mesh*

Figure 2.8: *Mesh visualizations showing mesh refinements and distribution at the vehicle centreline and around the tyres*

to the modelling of the lateral grooves.

2.5.3 IDDES

The IDDES simulations, performed in STAR-CCM+ (v11.06), allow for partially resolving large turbulence scales in the flow field. It utilizes a hybrid RANS-LES approach, which models the turbulence in the vicinity of the boundaries using RANS k-omega SST, while resolving it with LES elsewhere in the domain. The IDDES formulation can be found in [47] and is used with 2^{nd} order temporal discretization and 2^{nd} order upwind spatial discretization. The Hybrid Gauss - Least Square (Gauss-LSQ) method is used for gradient discretization with second order accuracy. The flow is assumed to be isothermal and incompressible. All unsteady simulations are initialized with their respective steady state k-omega solutions. The timestep has been slowly ramped down from $5x10^{-3}$ s over 3 s of physical time to reach its final value of $2x10^{-4}$ s with six inner iterations. Then, the flow and forces are averaged over an averaging interval of 2 s. These time step and averaging interval durations have been determined after a sensitivity analysis, briefly presented in the results section and Paper F.

The simulation domain for the full vehicle is 70 x 20 x 10 m with a uniform velocity inlet of 100 km/h and a pressure outlet. The ground motion is represented by a moving wall boundary condition and the remaining domain surfaces are set to symmetry planes, resulting in a slip wall boundary. The rim spokes are modelled with sliding mesh for

all vehicle simulations resulting in approximately 1 degree of rotation per timestep, and around 14 rev/s. The remaining rim surface, tyre surface, and rain grooves are modelled with Rotating Wall approach. The lateral grooves have been investigated both using Rotating Wall and MRFg approaches, and are compared in the results and Paper E. Figure 2.9 shows the mesh and the domain boundary conditions.

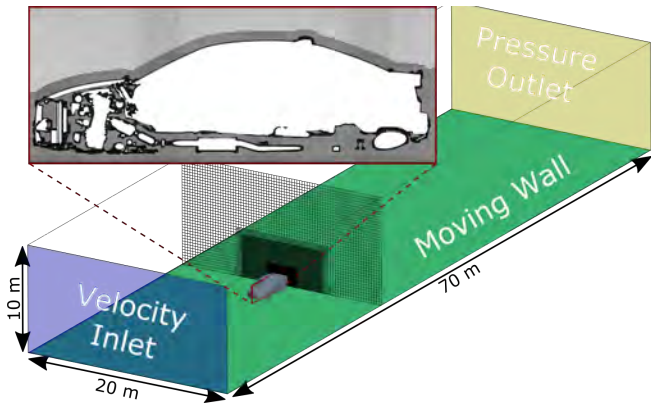

(a) *Vehicle domain and mesh planes*

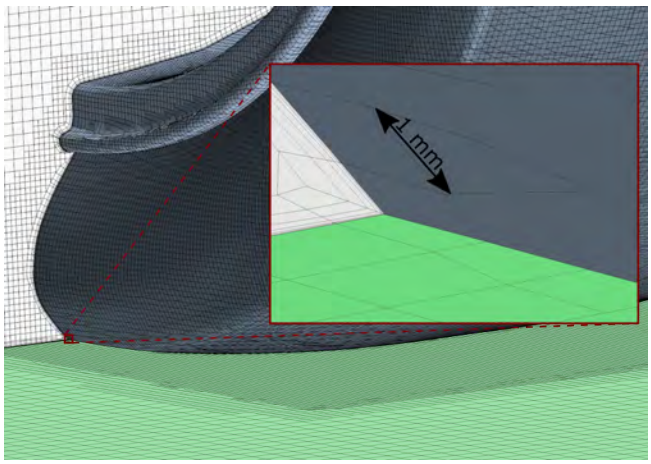

(b) *Mesh refinement around the wheels and contact patch*

Figure 2.9: *The domain for the full vehicle IDDES simulations with a sample mesh planes showing the mesh around the car (a) and at the wheel contact patch (b).*

2.6 Results and Discussion

This section presents the most important results obtained throughout the work. It is distributed by topic which allows for connections to be made across the various simulations and experiments.

2.6.1 MRFg

The first investigation of MRFg presented in [2], showed promising results when comparing to other rotation modelling methods. The changes in drag and lift coefficients, when two different patterns with lateral grooves are introduced on a slick tyre, can be seen in Figure 2.10. The increase in drag when using Rotating Wall is significantly larger than the resulting increase with Sliding Mesh. Furthermore, the MRFg approach shows that it could reproduce similar drag changes to SM.

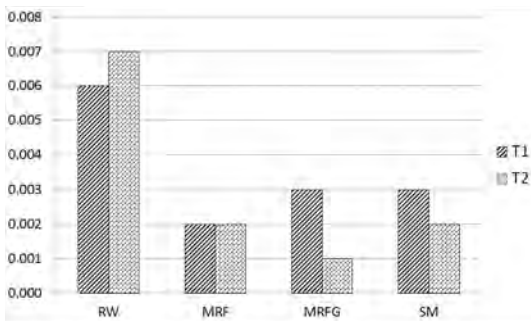

(a) *Delta C_d*

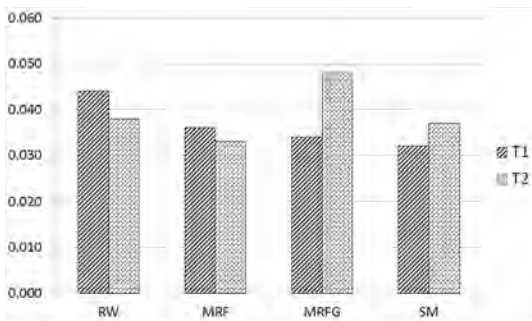

(b) *Delta C_l*

Figure 2.10: *Changes in C_d and C_l of the vehicle when using different modelling methods for tyre rotation on a closed rim and referenced to T0*

However, a more practical MRFg implementation has been later investigated with a

sensitivity analysis performed on an isolated wheel setup. The flow in this case was driven by the wheel rotation, and the main goal was to reproduce the Sliding Mesh velocity profile at the lateral grooves. Figure 2.11 shows how the MRFg implementation on the tyre (Figure 2.11c) produces a similar flow to the Sliding Mesh approach (Figure 2.11a). As expected, the Rotating Wall approach resulted in an incorrect velocity field inside the lateral grooves, (Figure 2.11b). This incorrect velocity with RW also results in lower velocities outside of the lateral grooves.

Given the significant improvements the MRFg method offers over a traditional RW, when modelling tyres with lateral grooves, both are applied to tyres in full scale vehicle simulations. As the vehicle in this case is in contact with the road, it was not possible to implement sliding mesh on the tyre, however the results are instead compared to experiments. The predicted change in drag, from adding patterns with lateral grooves on slick tyres, with closed and open rim configurations, are compared between CFD simulations and wind tunnel tests. The difference between the numerical and experimental predictions can be described as

$$\Delta\Delta\, C_{d\,conf} = (C_{d\,conf} - C_{d\,Slick})_{CFD} - (C_{d\,conf} - C_{d\,Slick})_{WT} \tag{2.4}$$

where $C_{d\,conf}$, is the drag for the configuration of interest and $C_{d\,Slick}$ is the drag when changing to a slick.

Figure 2.12 shows the significant improvement the MRFg method provides over RW, at no additional simulation cost. Although the change is slightly outside the uncertainty margins for the closed rim configuration, it is still significantly better that the RW approach result.

2.6.2 Lateral Grooves

As explained in Section 2.2 and Section 2.6.1, the modelling of the lateral grooves is important for obtaining good agreement with experiments. In Paper A, the lateral grooves, or edge pattern, were modelled using the rotating wall approach. They generally contributed to an increase in drag, however in certain cases the drag increase was quite large. The process of investigating the lateral grooves modelling then began and the MRFg method was developed and analysed.

The change in drag from adding lateral grooves, modelled with the MRFg method has then been studied and compared to experiments in Paper E. The results are summarized in Figure 2.13.

The simulations consistently predicts an increase in drag which is not always present in the wind tunnel tests, especially for the closed rim (CR) configurations. Generally speaking, the closed rim has consistently proven to be more difficult to predict with the absolute drag values being strongly under predicted in CFD by around 11-14 drag counts. On the other hand the open rim was predicted within 4 drag counts for all tested configurations. The causes for this under prediction are not currently clear but the effects

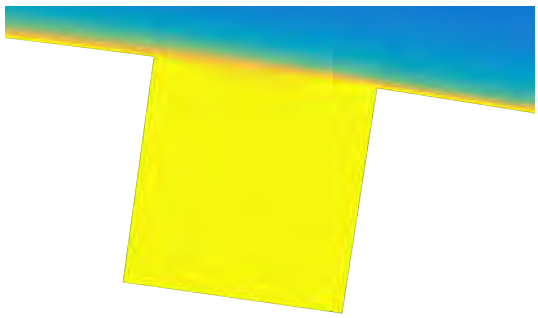

(a) *SM both tyre and grooves*

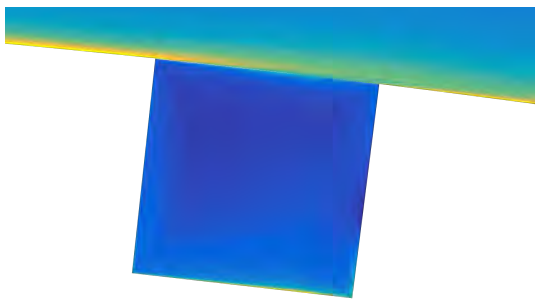

(b) *RW both tyre and grooves*

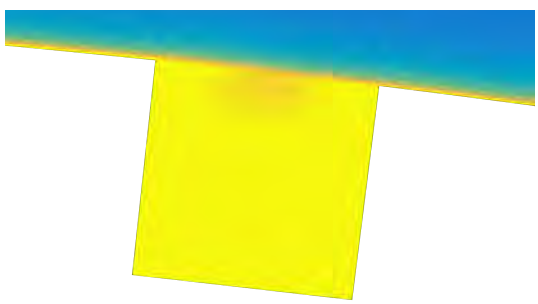

(c) *MRFg - RW tyre and MRF grooves*

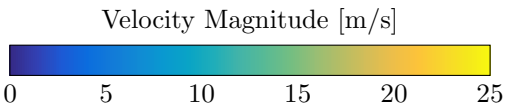

Figure 2.11: *Instantaneous velocity field in a plane cutting through one of the lateral grooves. The clockwise tyre rotation drives the flow left to right along the tyre surface.*

of the wind tunnel geometry, boundary layer control system, struts, tyre side wall details, and contact patch are all possible causes for this deviation.

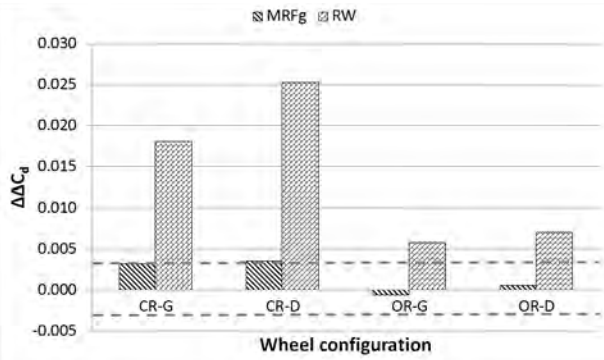

Figure 2.12: *$\Delta\Delta C_d$ for various wheel configurations using MRFg and RW. The dashed lines present uncertainty margins. The wheel configurations are CR-G (Closed Rim with Grooved tyre), CR-D (Closed Rim with Detailed tyre), OR-G (Open Rim with Grooved tyre), and OR-D (Open Rim with Detailed tyre).*

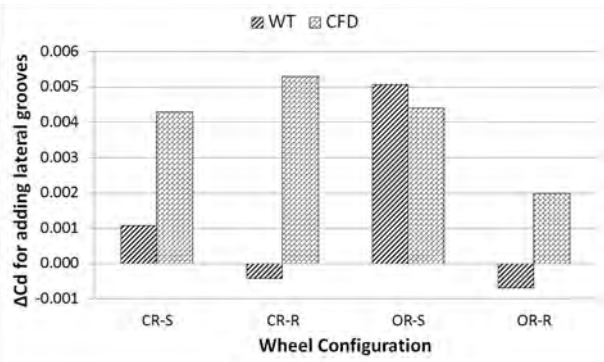

Figure 2.13: *The change in drag when introducing lateral grooves on various wheel configurations from wind tunnel tests and CFD simulations.*

In simulations, the lateral grooves introduced small vortices into the flow at the front wheel which merged into the contact patch separation and increased the drag of the vehicle. From looking at the cumulative drag development over the vehicle, the increase in drag could be seen locally around the front wheel with no changes or interactions further downstream. Figure 2.14 shows the q-criterion, as defined by Hunt, Wray, and Moin [48], isosurface around the front wheel where the vortices could be identified at the lateral grooves.

2.6.3 Rain Grooves

The rain grooves have been investigated in terms of their geometrical representation in CFD as well as their effects on the overall vehicle forces. The first step in the analysis

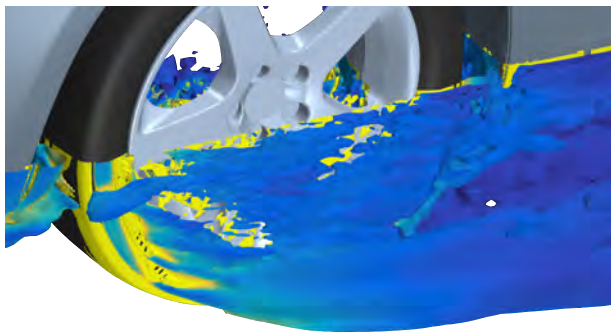

(a) *Open rim slick (OR-S)*

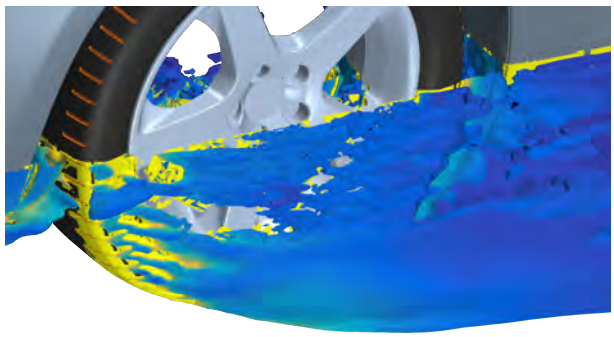

(b) *Open rim lateral grooved (OR-G)*

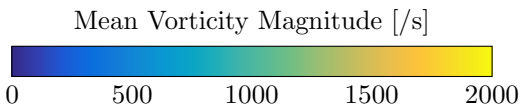

Figure 2.14: *Isosurface of Q-criterion at $5000/s^2$ coloured by mean vorticity magnitude around the front left wheel.*

was to look into their representation at the contact patch. As the tyres deform at the ground, the deformation needs to be replicated in CAD to represent the physical object. Typically such a deformed tyre geometry is not readily available and aerodynamicists need generate a simplified representation. An important factor in the deformation of the rain grooves is their continuity at the ground. Preserving the grooves versus cutting them off at the ground has been investigated in Paper A. The drag and lift coefficient changes due to adding the rain grooves on a slick tyre are summarized in Table 2.2.

The predicted drag increase, when the rain grooves are cut, changes to a decrease in drag when they are preserved. In this case, the predictions are about 10 counts apart which is very significant. A similar trend could be seen for the lift predictions. The different effects the rain grooves have can be better understood when looking at the pressure distribution on the front left wheel, presented in Figure 2.15. In Figure 2.15a, the rain grooves are cut

Table 2.2: *Changes in drag and lift coefficients when adding rain grooves on a slick tyre using different representations at the contact patch.*

	Drag	**Lift**
Cut at contact patch	+0.006	+0.009
Preserved at contact patch	-0.004	-0.024

and a high pressure spot is visible upstream of the contact patch. This spot is significantly reduced when the grooves are preserved in Figure 2.15b, as they connect the high pressure spot to the low pressure downstream of the contact patch. The flow accelerates through the grooves thus generating the low pressure within them shown in Figure 2.15b.

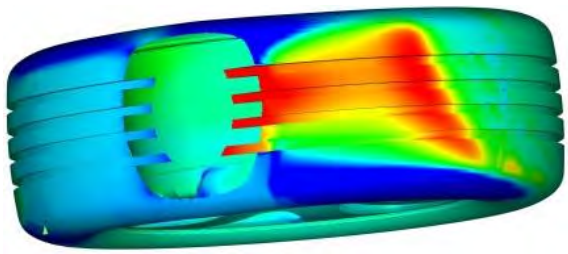

(a) *Cut rain grooves*

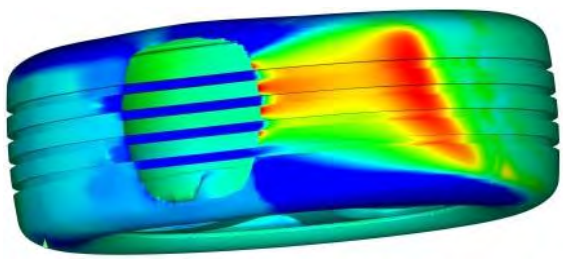

(b) *Preserved rain grooves*

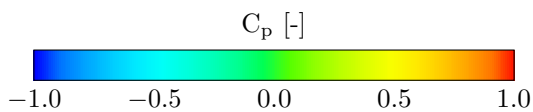

Figure 2.15: *Pressure distribution on the front left tyre from a bottom view. The flow direction is from right to left. The part of the tyre which is cut away is the contact patch, where the tyre is in contact with the ground.*

The changes in drag and lift coefficients resulting from adding rain grooves, on four different tyre configurations and four different rims, have been simulated in Paper A. The results can be seen in Figure 2.16. The general trend shows a small reduction in drag and

a large reduction in lift.

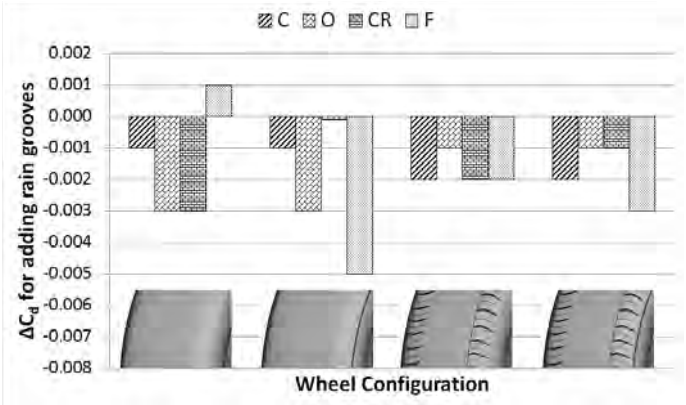

(a) *Overall C_d change*

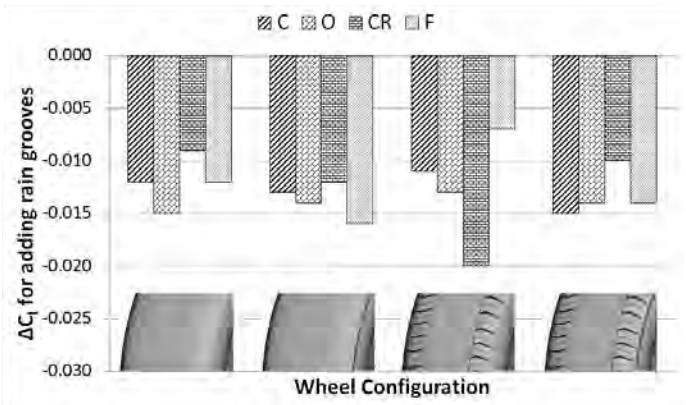

(b) *Overall C_l change*

Figure 2.16: *Overall change in vehicle aerodynamic coefficients when main grooves is added on different tyres and different rims*

These changes have been reproduced in a later work, Paper F. Figure 2.17 shows the change in drag when adding the rain grooves is tests and simulations. For most configurations, a clear reduction in drag is obtained with a good match between tests and simulations. However, the lift is not well predicted with the simulations clearly over predicting the reduction in lift.

The significant reduction in lift in CFD, is to a large extent a result of the flow accelerating through the rain grooves at the contact patch. Since it can be traced directly to the grooves, a problem presents itself: the low pressure in the grooves also creates a lift force on the ground. This is not reported in the CFD simulation, yet in the wind tunnel the

contact patch is over the wheel drive unit, on which lift is measured. Although a general lift correction is applied in the tunnel to correct for the wheel drive unit measurements, this does not take into account the tyre geometry. Since the lift at the ground counteracts the downforce generated on the rain grooves, a more comparable change in CFD can be obtained. This is done by including the ground surface within the contact patch in the lift reporting, seen in Figure 2.17b. The lift predictions are significantly improved and most configurations are now well predicted apart from the open rim with lateral grooved tyres, OR-G. The change in pressure distribution on the wheel drive units is another effect measured in the wind tunnel which is not present in CFD, or on road. This aspect is worth future investigations for more accurate lift comparisons between different tyres.

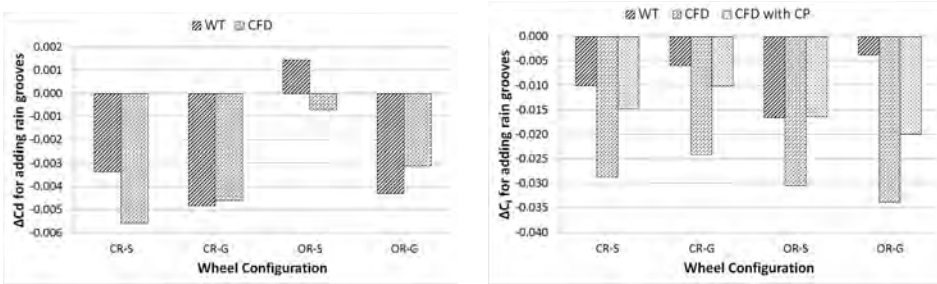

(a) *Overall C_d change* **(b)** *Overall C_l change*

Figure 2.17: *The change in drag wand lift when introducing rain grooves on various wheel configurations from wind tunnel tests and CFD simulations.*

The reduction in drag due to the rain grooves is a result of how the grooves alter the flow around the underbody. At the front wheel, the separation at the contact patch is reduced when the rain grooves are present and the vortex in the left bottom corner in Figure 2.18a is suppressed. However, the vortex directly downstream of the wheel becomes stronger. At the rear wheels a vortex is created resulting in an insweep of the flow towards the rear wake. The vortex can be identified in Figure 2.18d and its presence is accompanied with an increase in base pressure, which leads to the reduction in drag further elaborated on in Paper F.

2.6.4 Sensitivity Analysis

For the latest simulations presented in Papers E and F, numerous investigations have been performed in order to evaluate their sensitivity in predicting the desired coefficients and moments. The investigations covered mesh changes, time step size, and averaging interval duration, and number of inner iterations per time step. The investigations have been performed on the full vehicle, with closed rim and slick tyres.

The mesh refinement studies on the full vehicle looked at changing the growth rate of the prism layers. This has been achieved by keeping the total height of the prism layers fixed

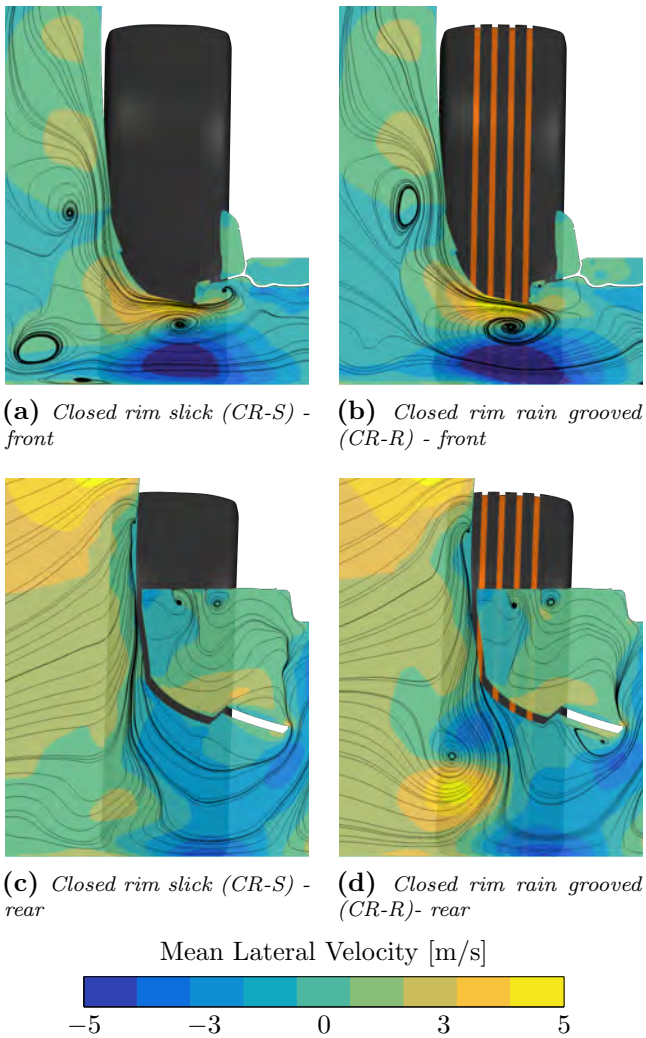

(a) *Closed rim slick (CR-S) - front*

(b) *Closed rim rain grooved (CR-R) - front*

(c) *Closed rim slick (CR-S) - rear*

(d) *Closed rim rain grooved (CR-R)- rear*

Figure 2.18: *Mean lateral velocity in a plane 0.5 m behind the front(top) and rear(bottom) left wheel centres with in-plane streamlines for slick(left) and rain grooved(right) tyres on a closed rim.*

whilst increasing the number of cells. It allows for minimizing changes to the volume mesh outside of the layers. However, the aspect ratio between the last prism layer cell and first volume cell is slightly affected. For the investigated configurations, this change has been overlooked as it was quite small. The prism layer growth ratios investigated are 2.0, 1.7 and 1.5. The change in drag observed was small, less than 2 counts between the three configurations. Similar results were obtained when the prism layers and surface

mesh size where kept constant, while a slower mesh refinement into the volume was implemented. This tested whether the transition to coarser volume mesh was affecting the results. However, the overall changes in drag and lift as well as their development over the length of the car did not change significantly.

The time step studies investigated four different time steps: $4x10^{-4}$, $2x10^{-4}$, $1x10^{-4}$, and $5x10^{-5}$ seconds. The latter results is a CFL number of 1 in almost all cells in the domain and its results should be reproduced if a coarser time step is to be used. The results showed good reproducibility for both the $2x10^{-4}$ and $1x10^{-4}$ seconds. However, the $4x10^{-4}$ drifted away slightly with a 3 counts change in drag and a 16 count change in lift. The drag prediction was within one count for the $2x10^{-4}$ and $1x10^{-4}$ seconds. From the presented results the $2x10^{-4}$ seconds had been selected. Yet, is a relatively large time step resulting in one degree of rotation for the sliding mesh regions and CFL numbers around five in most cells around the vehicle. For that purpose it had to be confirmed that the solution was converging per time step. The number of inner iterations was investigated with 6 and 8 inner iterations yielding negligible differences. It might have been possible to reduce the number of inner iterations even further however this has not been investigated.

The averaging time investigation has been performed by running a simulation for a total of 7 seconds with the last four seconds considered for the averaging interval study. As the drag and lift history for the last four seconds is obtained, various averaging intervals could be studied. For example the drag and lift for the first two seconds, last two seconds, or the middle two seconds were averaged all giving the same result. This enhanced the trust that the initialization is not affecting the final results. Still, in order to check for repeatability, the simulation has been performed again from the beginning with only 5 seconds total physical time, with the last two seconds being the averaging time. The results again confirmed that 2 seconds were enough to obtain an accurate prediction of drag and lift.

A summary of some of the most notable tested configurations is presented in Table 2.3.

Table 2.3: *A short summary of the most notable methodology investigation results. They are presented as deltas to the reference setup.*

Change from reference setup	ΔC_d	ΔC_l
Prism layer Growth 1.7	0.001	0.005
Prism layer Growth 1.5	0.002	0.007
Refined Volume Mesh	0.001	-0.005
Time step of $4x10^{-4}$ s	-0.004	0.016
Time step of $1x10^{-4}$ s	0.000	0.005
Time step of $5x10^{-5}$ s	-0.001	0.000
Averaging interval of 4 s	-0.000	+0.000

Chapter 3

Cooling Flow

3.1 Background Information

Cooling flow plays a large role in optimization of vehicles as it significantly changes the flow around the car. Its effect on drag is referred to as cooling drag. For practical purposes, cooling drag is measured as the difference between open and closed cooling inlets[49]. Thus cooling drag includes numerous effect such as, the pressure drop across the cooling package, interference drag, momentum change, leakage effects. It can be described in various ways [50–53]. These different interactions make it very complex to validate CFD simulations to wind tunnel experiments. However, the mass flow through the radiator and the force acting on it are quantities which can be isolated from other interferences both in tests and simulations. For that purpose, This work utilises load cells to measure the forces acting, on a simplified cooling package, and compare them to simulations. Furthermore, given the availability of the force measurements, an investigation into using it to calculate mass flow is also performed.

Traditional approaches, for measuring cooling flow, rely on measuring fluid properties such as pressure or velocity. Pressure measurements are achieved using pressure probes. This requires two pressure measurements. If two static pressures are measured then a pressure drop across the core can be calculated. If one total and one static pressure are measured then the dynamic pressure can be calculated. Both methods allow for the measurement of the velocity over that point. Some different setups utilizing this method in application can be seen in many works [54–56]. Velocity measurements are achieved using anemometers. This can be achieved using hot wires where the cooling rate of the wire indicates the air flow velocity. It can also be simply achieved by placing small propellers in the air flow and the speed of the propeller rotation indicates the velocity of the air. Some different setups utilizing this method in application can be seen in many works [54, 57, 58]. These methods usually result in a measurement of the average velocity

over a certain area, yet there usually still exist gaps between the measurement samples which require interpolations or assumptions. A combination of pressure and velocity measurements is also performed by Williams [59], thus providing improved measurement accuracy and reducing the sampling error.

Most traditional approaches require multiple measurements to be performed at many local points around the radiator core. With an increase in measurement points comes not only an increase in accuracy but also an increase in equipment blockage, which alters the flow, as well as an increase in measurement equipment demand. Also going from these local measurements to the global mass flow, introduces additional interpolation and discretization uncertainties.

However the alternative force based approach quantifies the air flow through the radiator core, globally, without the need for multiple local measurements. The approach relies on measuring the physical effects of the air flow on the core; thus looking at the resultant force acting on the radiator core. From the force, the air mass flow is calculated.

3.2 Experimental Setup

The experiments aimed at measuring the air mass flow rate through a vehicle radiator using two different methods. The first method is a traditional one which is commonly used in vehicle aerodynamics applications. The second method is a novel approach developed by the author.

The pressure based method relies on placing several pressure probes across the radiator core. The probes are similar to a Prandtl tube where the output from each is a total pressure and a static pressure at the measurement point. Using this information the dynamic pressure can be computed and thus the the local velocity through the pressure probe is obtained. However, as the geometry of the probe is not similar to the geometry of the radiator fins, this local probe velocity needs to be corrected. For that purpose, a calibration test needs to be performed in a test rig, where a uniform flow through the radiator can be obtained and measured externally by the rig's measurement system. Each pressure probe is calibrated separately to the average velocity across the radiator core. When test measurements are performed, each probe measurement is corrected differently using its own calibration curve, then these local measurements are used to interpolate/extrapolate over the rest of the radiator core resulting in a velocity distribution. By integrating this distribution the volumetric flow rate is determined.

A DTC Initium data acquisition pressure system has been used for pressure measurements in the test rig. Two 32 port ESP scanners are used thus giving a total of 64 pressure measurements. As there are 48 probes in the radiator, a total of 96 pressure measurements need to be performed to get the capture the flow over the whole radiator. For that reason all tests in the rig where performed twice with one of the blocks alternating on different probes while the other maintains a fixed position for monitoring repeatability. The probes used for the measurements are the Ruijsink micro probes [55] which are shown

in Figure 3.1 along with the pressure system used.

(a) *DTC Initium data aqusition unit* **(b)** *ESP pressure scanner* **(c)** *Ruijsink micro probe*

Figure 3.1: *Measurement equipment used in the test rig*

The calibration test has been performed at the Volvo GTT Fan Test Rig facility where the pressure drop vs. volumetric flow rate of the radiator has been empirically obtained. The test rig a closed loop plenum to plenum test rig, with the outlet chamber maintained at atmospheric pressure. The pressure drop is measured plenum to plenum and the air mass flow is measured by 6 venturi type nozzles (ISA 1932). Combinations of open and closed nozzles are used for different target mass flows in order to operate the nozzles within their correct Reynolds number range. More detailed information on the rig is available in Gullberg [60]. A schematic of the rig is shown in Figure 3.2 while the radiator setup is shown in Figure 3.3.

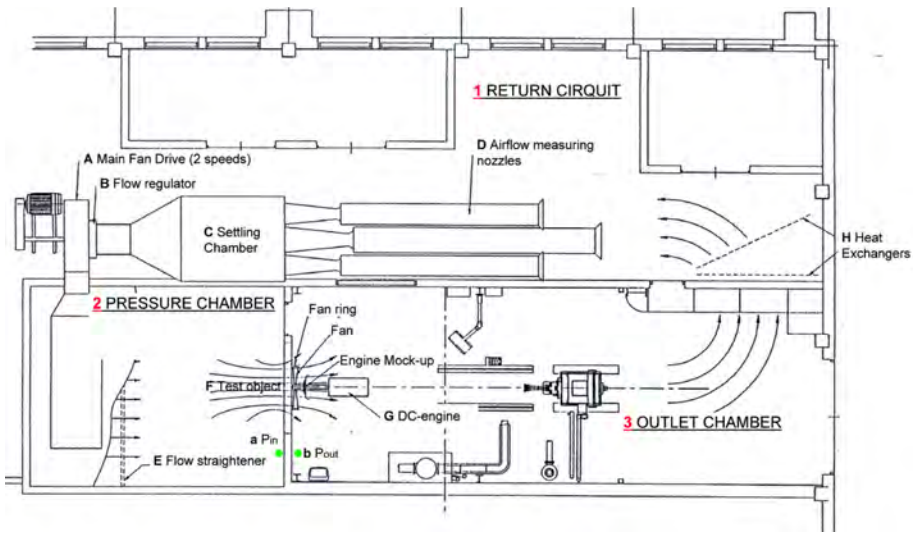

Figure 3.2: *Schematic fan test rig*

(a) *radiator set up in the pressure chamber*

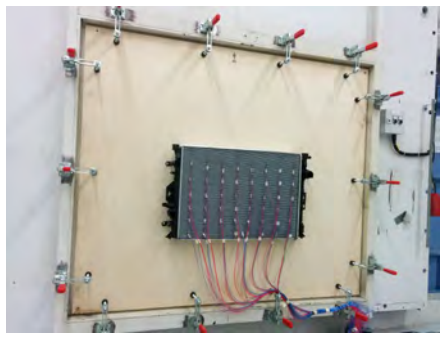

(b) *outlet chamber*

Figure 3.3: *Measurement equipment used in the test rig*

The force based method relies on measuring the force acting on the radiator core and then calculating the velocity through the radiator. In order to do that the pressure drop vs. volumetric air flow rate curve needs to be empirically extracted in the fan test rig. This curve can be converted into a force vs. average velocity as the force is a result of the pressure drop integrated over the core area and the volumetric air flow rate is a result of the velocity integrated over the same core area. One can also notice that volumetric flow rate, mass flow rate and average core velocity are interchangeable terms with only constants separating them, following the 1-D equation of continuity presented in Equation 1.1.

$$\dot{m}_{core} = \dot{V}_{core} \times \rho_{air} = v_{average} \times A_{core} \times \rho_{air} \tag{3.1}$$

The wind tunnel facility used for this investigation is the Volvo Aerodynamic Wind Tunnel available at Volvo Cars, shown in Figure 3.4. It is a closed loop wind tunnel powered by a 5MW fan achieving speeds up to 250 km/h in the 27 m^2 test section. The tunnel delivers a free stream with turbulence intensity below 0.1 % and less than 0.6 degrees deviation from main flow direction [46]. More information on the wind tunnel can also be found in Section 2.3. The pressure system used at the wind tunnel is a PSI 8400 system with PSI ESP miniature electronic pressure scanners.

The vehicle used in the test is a Volvo S60 production car. However for the purpose of this investigation some modifications had to be performed to the engine bay. For validation purposes, only one radiator is placed inside the vehicle as to have only one pressure drop. The radiator was suspended on load cells which attached the water tanks to the vehicle chassis. All components between the radiator and the front bumper were removed. All components connected to the radiator water tanks were removed except for the fan shroud which instead was mounted to the vehicle chassis. The fan was removed from the shroud. Also custom made aluminium ducts sealed the grill and spoiler inlets from the bumper to the radiator core, thus shielding out the water tanks. This allows the load cells to measure the force acting on the radiator core with minor influence from forces on the water tanks.

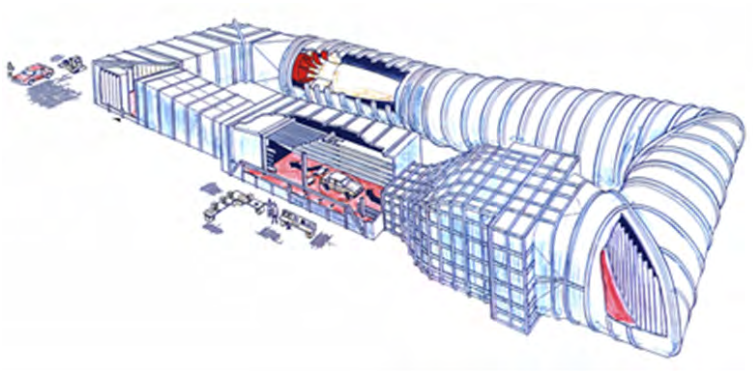

Figure 3.4: *Volvo Cars Aerodynamic Wind Tunnel*

Figure 3.5 shows the radiator mountings on both sides of the water tanks connected to the chassis while Figure 3.6 shows the Reference configuration with the aluminium ducts sealing the bumper to the core.

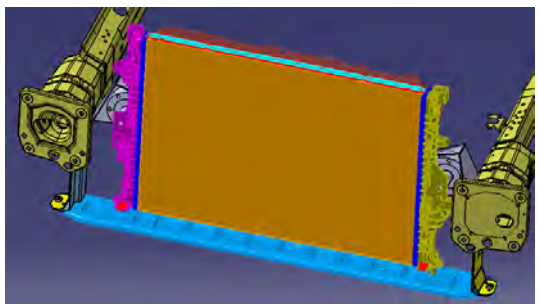

Figure 3.5: *Radiator mounting on load cells*

Different grill configurations have been tested in the tunnel to demonstrate the usability of the new method and compare it to probe measurements. The spoiler opening, in the lower part of the front bumper, has been left completely open for all tests, as shown in Figure 3.6. The aim of the test is to vary inlet blockage in order to evaluate the method's ability to predict the mass flow with different flow distributions. The Reference configuration is the minimum blockage configuration after which blockage starts increasing with Grill 1, 2, and 3 until reaching a Closed Grill. A realistic grill has been also tested for benchmarking purposes. The configurations investigated are shown in Figure 3.7 in order of increasing blockage (top to bottom, left to right).

For each configuration, measurements were performed as continuous sweeps of increasing velocity from 80 km/h to 200 km/h in increments of 20 km/h to analyse the effects of velocity variations.

Figure 3.6: *Reference configuration showing the aluminium ducts*

(a) *Grill 1: Open grill*

(b) *Grill 2: Production grill*

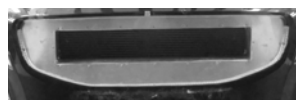

(c) *Grill 3*

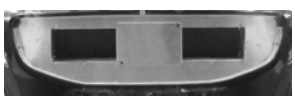

(d) *Grill 4*

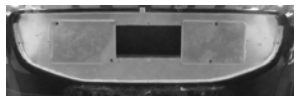

(e) *Grill 5*

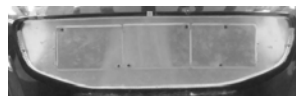

(f) *Grill 6: Closed grill*

Figure 3.7: *The different grill designs sorted by blockage ratio from completely open to completely closed*

3.3 Simulation Setup

3.3.1 Geometry Representation

The virtual vehicle geometry is a detailed model of the test object. Although not all details could be guaranteed to be a perfect match, the radiator brackets, load cells, grill configurations, and ducting have been reproduced following numerous measurements. The vehicle model includes the leakages around the bumper beam area, however the ducting is air tight at the radiator. Different views of the radiator assembly in the virtual model are presented in Figure 3.8.

In order to capture the small details and air leakages, the radiator assembly is meshed with 1.25 mm cells with large refinement zones of 2.5 mm around all flow inlets and outlets. This includes both front bumper inlets, wheelhouse openings, and exhaust tunnel outlets.

The simulations have been performed both in open road conditions, a large oversized domain, as well as in a virtual model of the physical wind tunnel. The open road and virtual tunnel setups can be seen in Figure 3.9, and they resulted in mesh sizes around

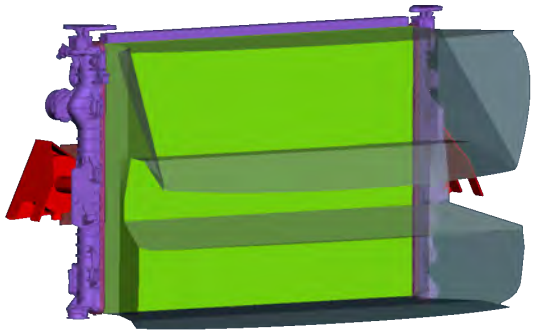

(a) *Iso view*

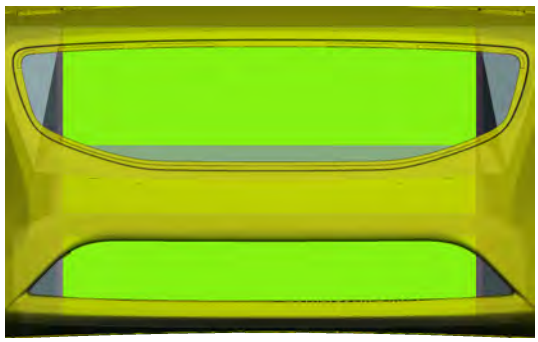

(b) *Front view*

(c) *Rear view*

Figure 3.8: *The radiator assembly as seen from different views.*

(a) *Open road*

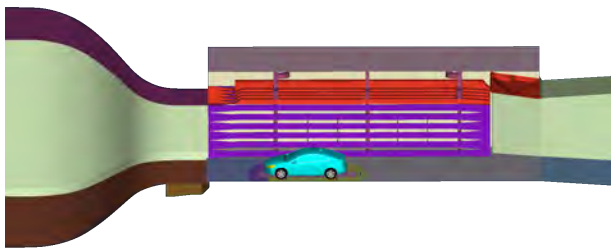

(b) *Virtual tunnel*

Figure 3.9: *The test vehicle in: (a) open road, (b) virtual wind tunnel conditions.*

190 and 320 million cells, respectively.

3.3.2 Solver Settings

The simulations are performed in FLUENT (v16) using the steady state RANS k-epsilon turbulence model. Enhanced wall treatment is applied at the wall and the Green-Gauss node-based scheme is used for gradient discretization. The pressure, momentum, turbulent dissipation rate, and turbulent kinetic energy discretization are all of 2^{nd} order accuracy.

The radiator has been modelled as a porous region with the viscous and inertial coefficients obtained from the fan test rig. The rim spokes are modelled using the MRF approach. The simulations are performed for a vehicle velocity of 100 km/h both in the open road conditions and in the virtual wind tunnel.

3.4 Results and Discussion

This section presents some findings and observations from Papers C and D. The main highlights are the effects of the wind tunnel blockage on cooling flow measurements, the effect of discretization on mass flow measurements, and analysis of the force based method.

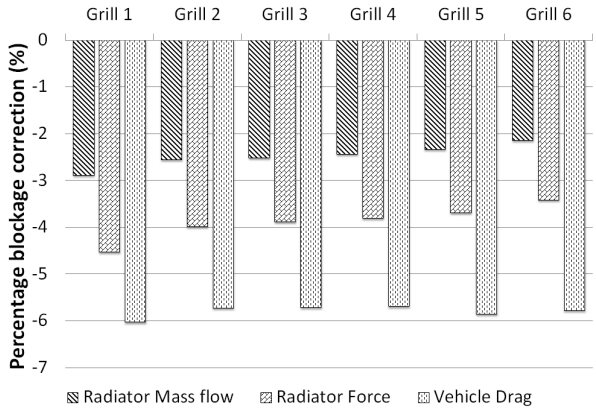

Figure 3.10: *Percentage blockage correction needed to convert virtual tunnel quantities to their equivalent open road values.*

3.4.1 Tunnel Blockage Effect

The wind tunnel is a controlled environment designed to allow for the measurement of various aerodynamic forces. However, it typically introduces different forms of blockages which require corrections to be made. The specific corrections required for the wind tunnel used for this work can be found in [61]. In order to represent on road conditions, the wind tunnel tests performed in this work, require a 6 % reduction of the measured drag forces. This required correction has been well reproduced in CFD, where the drag forces for open road conditions were around 6 % lower than the respective configuration in the virtual wind tunnel. The drag force was not the only quantity affected, the force acting on the radiator core as well as the mass flow through the radiator followed the same trend, shown in Figure 3.10. This suggests that the radiator force and mass flow, measured in experiments, need to be corrected by around 4 % and 2.5 % respectively to be comparable to open road simulations. It should also be mentioned that the percentage reduction is grill configuration dependent and it decreases gradually between Grills 1 to 6.

3.4.2 Measurement Grid Effect

The pressure measurements utilize a 48 probe grid in order to estimate the mass flow through the radiator. This requires a form of interpolation/extrapolation of these 48 local measurement points over the radiator face area. However in the CFD simulations, a much finer discretization grid is obtained, about 250,000 points. This introduces problems in the comparison between CFD and wind tunnel tests.

In order to get a more consistent comparison, a 48 virtual probe grid was extracted from CFD and used for calculating the mass flow similarly to experiments. This also allows for investigating the effect of the measurement grid on the overall results. Qualitatively, this

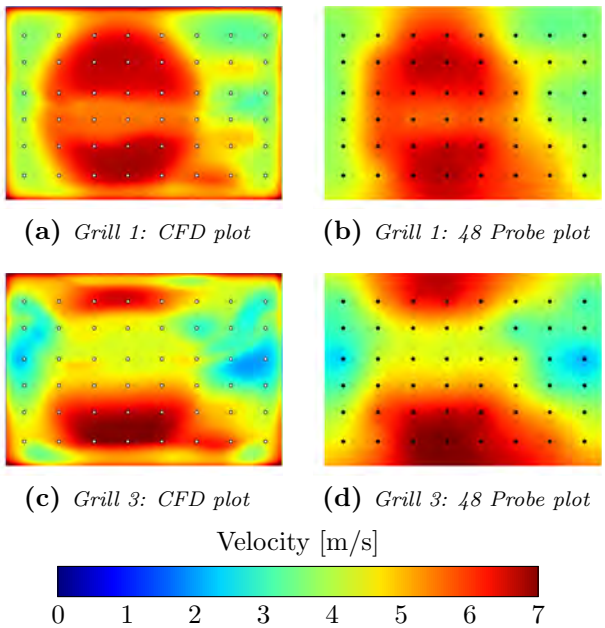

(a) *Grill 1: CFD plot* **(b)** *Grill 1: 48 Probe plot*

(c) *Grill 3: CFD plot* **(d)** *Grill 3: 48 Probe plot*

Figure 3.11: *Comparison of numerical velocity distribution for two different grills when plotted directly from CFD vs. plotted using only 48 measurement points similarly to experiments.*

can be seen in Figure 3.11. The velocity distribution is generally blurred out when the 48 probe grid is used. The flow outside of the grid is significantly altered as the values are extrapolated from the interior measurement points. The 48 grid effect on mass flow showed no specific trend and the total mass flow could be altered by around 2 %, for the simulated configurations. Given the inconsistent trend, these errors could add up when comparing two configurations. For example, Grill 3 has 6.3 % lower mass flow than Grill 1 when comparing the mass flows obtained from the CFD plot. Yet, when using the 48 probe plot, then Grill 3 is 9.6 % lower in mass flow than Grill 1.

3.4.3 Force Based Mass Flow Measurement

The main challenge in predicting mass flow comes from the relation between the force and mass flow, which is not linear but rather described by a second order polynomial. As a result the average force acting on the radiator will always over predict the average velocity through it. This over prediction needs to be corrected for, thus introducing some uncertainties. An example of this over prediction is shown in Figure 3.12, where the colour yellow depicts two velocity measurement points. The green line represents the results if one would look at the velocity average. The purple lines represent the results if one would look at the force average. As observed, the average velocities using the different

approaches do not match. The force averaging causes an over prediction of 0.5 m/s in average core velocity. This is equivalent to a 4 % over prediction of the mass flow.

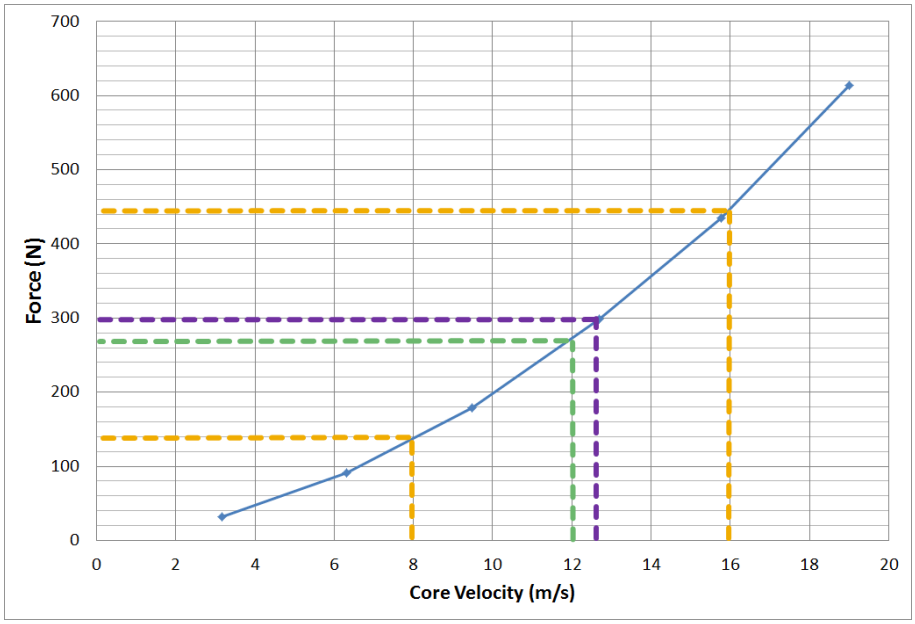

Figure 3.12: *Over prediction demonstration on force versus velocity curve*

In Figure 3.13, the force measurement shows the expected over prediction of the velocity compared to the probes. Comparing to Figure 3.7, for grills with low blockage, like grills 1, 2, and 3, the mass flows predicted by the force is already within the measurement uncertainty of the pressure probes. However as the blockage increases the over prediction increases as shown for Grills 4, 5, and 6. This is mainly due to the increase in flow inhomogeneity through the radiator.

The velocity distributions through the radiator core, for the different grill configurations along with the respective inhomogeneity values, are shown in Figure 3.14 for a testing velocity of 200 km/h.

The equation for calculating inhomogeneity used in this work is taken from Hucho [49] and is described as

$$i = \frac{1}{n} \sum_{k=1}^{n} \frac{\left| \dot{m}_K \frac{A_R}{A_K} - \dot{m}_{tot} \right|}{\dot{m}_{tot}} \tag{3.2}$$

where n is the number of measurement points, $\dot{m}_K$ is the mass flow through one area section, A_K is the size of one area section, A_R is the size of the radiator core area, and $\dot{m}_{tot}$ is the total mass flow through the radiator.

From the above, it can be noted that for grills with low inhomogeneity the force based

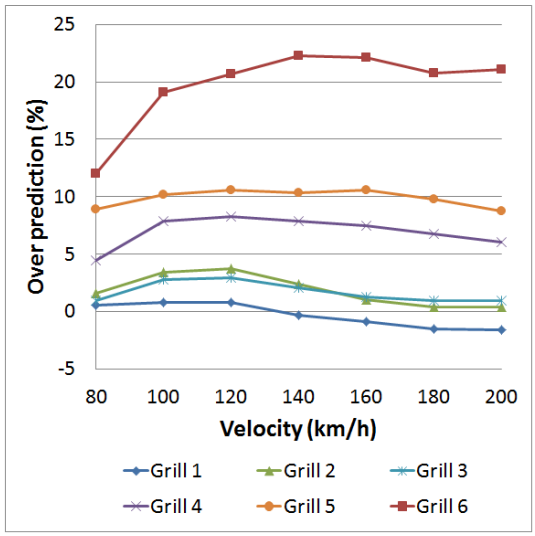

Figure 3.13: *Percentage over prediction comparing v_{avg_F} to v_{avg_P}*

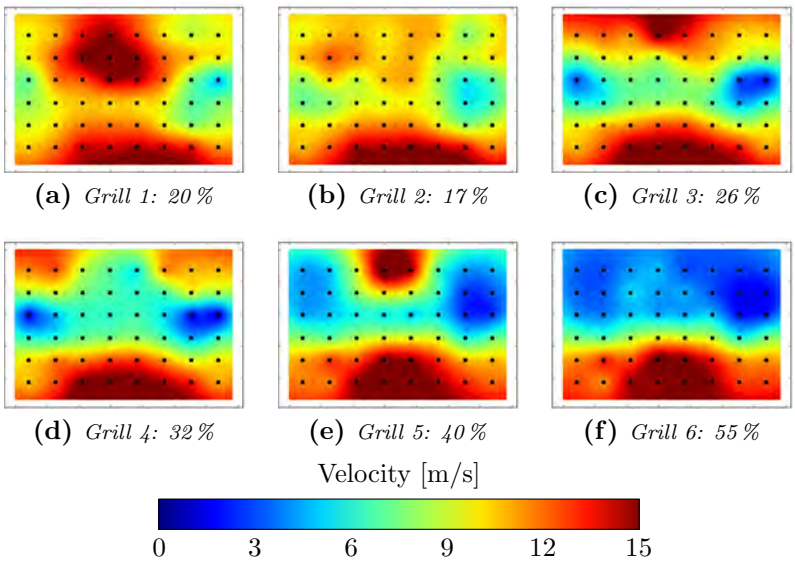

Figure 3.14: *Velocity distribution through the radiator core for the different grill configurations at 200 km/h testing speed. Inhomogeneity values are also presented for each plot.*

approach is able to produce comparable results to the utilized pressure based approach. However for high inhomogeneity, a correction is required. In Paper D, a correction method based on the migration of the centre from the geometric centre of the radiator of pressure

is suggested. A curve that relates the over prediction to the migration distance is required and should ideally be obtained from the fan test rig. However due to unavailability at the time, the curve has been computed using the pressure measurements. When the correction is applied, the force based measurements predicted the pressure based measurements within $\pm 4\,\%$. It should be noted that since the correction curve is extracted from the pressure measurements it naturally influences the results. Hence, it cannot be confirmed that either the force based or the pressure based methods are indeed measuring the actual mass flow. It can only be concluded that they could produce similar results.

3.4.4 Wheel effects

Given the above setup, it was also possible to evaluate the effect of different rims and moving ground conditions on mass flow and cooling drag. For this purpose closed rims configurations were tested along with multiple variations of rotating and stationary wheels. However, no change in mass flow could be noted on neither the pressure based nor force based measurements. Further more it has been attempted to completely turn off the moving ground system, yet no changes could be observed there either. The cooling drag also did not vary significantly between the configurations. Hence, it was concluded that for this specific vehicle there is little to no interaction between the wheels and the cooling flow.

Chapter 4

Conclusion

4.1 Summary

The thesis presents a collection of works covering analysis of tyre aerodynamics, tyre rotation modelling, cooling flow measurements, and their effects on overall vehicle drag and lift. These subjects have been investigated using wind tunnel tests and CFD simulations.

A detailed analysis of two main tyre pattern features has been examined: the rain grooves and the lateral grooves. A hybrid rotation modelling approach, MRFg, has been proposed and implemented for modelling the lateral grooves. Comparison of the effects of different tyre features has been performed on two rim designs from both wind tunnel tests and simulations.

Cooling flow and radiator force measurements have been performed in the wind tunnel tests, using pressure probes and load cells. Then a method for quantifying cooling flow using the force measurements is also presented. From the CFD simulations, the effects of measurement grid and wind tunnel blockage effects are analysed.

The main outcomes from this work can be summarized in the following points:

- The lateral grooves can significantly affect the predicted drag, leading to erroneous results with incorrect modelling.
- The MRFg approach is able to significantly improve the prediction of drag change associated with the lateral grooves, compared to experiments, at no additional computational cost.
- When the rain grooves are preserved at the contact patch, a drag reduction of a few counts could be observed in both tests and simulations, along with a lift reduction in most cases.

- The force based approach for measuring cooling flow is able to predict the mass flow with comparable accuracy to the pressure based method, when the flow inhomogeneity through the radiator is low.
- The force based approach for measuring mass flow is relatively cheap, robust, and non-intrusive.
- The effects of wind tunnel blockage could result in up to 3 % over prediction of the cooling flow compared to on road conditions.
- The measurement grid in the pressure based method can alter the mass flow measurements by around 2 %.
- The cooling flow effects on vehicle drag and lift, as well as the fore acting on the radiator, matched well between tests and simulations. For this good match to be possible, the wind tunnel geometry has been included in CFD.

From the methodology and modelling investigations performed for CFD, it is recommended to:

- Model the rim spokes with the Sliding Mesh approach.
- Preserve the tyre pattern at the contact patch to be representative of the physical model.
- Model the tyre lateral grooves, and similar pattern details, with the MRFg approach.
- Keep the Courant number below 5 in the majority of the domain, along with minimum second order temporal and spatial discretization of all computed quantities.
- Include the wind tunnel geometry in the simulation when comparing to measured uncorrected quantities.
- Extract data from CFD with a similar grid resolution to measurement grids in experiments.

4.2 Future Work

From the conclusions presented above, a set of future investigations can be suggested:

- The MRFg method could be further analysed on the vehicle with flow field measurements from wind tunnel tests.
- The effects of the wheel drive units and contact patch area on lift predictions for different tyre patterns could be investigated, for comparable lift results between CFD and wind tunnel tests.
- The closed rim results were constantly under predicted in CFD in absolutes values. This requires further investigation to check whether this under prediction is connected to the difficulties in predicting the tyre changes for closed rims.

- Alternate corrections for the force based approach could allow the force based method to achieve more accurate results for cases with high inhomogeneity.

Chapter 5

Summary of Papers

5.1 Paper A

Investigation of the Influence of Tyre Geometry on the Aerodynamics of Passenger Cars

This work investigated the effects of different tyre geometry parameters on the overall drag and lift forces acting on the car. Using steady state numerical simulations, the effects of the tyre's deformation at ground contact, tyre's profile, various pattern features, and different rim designs were studied.

It was concluded that rain grooves on a tyre should be preserved at the tyre's contact patch and that the tyre profile can significantly influence results. Changes in pattern features have shown to be rim dependent and even spoke position dependent. The tyre features also showed larger effects on a sports wagon compared to a sedan with the same under body geometry. A reduction in drag and lift could be generally observed when the rain grooves are added. A significant increase in drag was noted when the side grove and edge pattern were added, however, this increase raised some concerns about the modelling of the edge pattern.

5.2 Paper B

Study of Different Tyre Simulation Methods and Effects on Passenger Car Aerodynamics

This work focused on rotation modelling, specifically to investigate the effects of modelling the lateral grooves, referred to as edge pattern in Paper A.

First, some general advantages and disadvantages of different rotation modelling methods are discussed. The methods are the Rotating Wall (RW), Moving Reference Frame (MRF), and Sliding Mesh (SM). The main take from this investigation was that RW is not able to produce the correct surface velocity when the velocity components are not tangential to the boundary surface. However, MRF is able to introduce such velocities, normal to the boundary, yet it will introduce certain errors of its own dependent on flow alignment and region size. For the purpose of correctly modelling tyres, a hybrid approach combining RW on the tyre surface and MRF in the grooves was introduced and referred to as MRFg.

Then RW, MRF, MRFg, and SM were implemented on two detailed tyre patterns, mounted on a closed rim on a simplified sedan type vehicle. In order to allow for SM, the car has been lifted so as to have the wheels floating 10 mm above ground. With this special setup, it was shown that MRFg provided promising results and comparable trends to SM. It was also shown that RW was over predicting the drag increase when introducing tyre patterns on slicks.

5.3 Paper C

Experimental and numerical investigations of cooling drag

This work investigated cooling drag, and flow, prediction in simulations and experiments. It also looked at different factors affecting this prediction such as wind tunnel blockage and measurement grid resolution. A special simplified cooling package setup was installed in the test vehicle. This allowed for mass flow measurements, using pressure probes, and radiator core force measurements, using load cells. The investigation covered six grill configurations with simulations performed in both an open road setup and a virtual wind tunnel setup.

The results showed that the wind tunnel blockage increases the mass flow through the radiator and the force acting on the radiator core across various grill designs. The measurement grid resolution, on the other hand, altered the mass flow in an inconsistent manner with the different velocity distributions.

Although the cooling flow predictions did not match well with the measured experimental values, for all grill configurations, the forces acting on the radiator were well within uncertainty margins for most. The cooling drag, front lift, and rear lift changes for the various grill configurations were well predicted when the vehicle was simulated in the virtual wind tunnel.

5.4 Paper D

Force Based Measurement Method for Cooling Flow Quantification

This paper describes a force based approach for quantifying cooling flow. First, the force acting on the radiator core is measured, and then, the equivalent air mass flow is calculated. In addition to direct force comparison to simulations, the force method offers various advantages like reliability, non-intrusiveness, and robustness. Its main disadvantage is that it inherently over predicts the mass flow and this is thoroughly described. This has been related to flow inhomogeneity and a correction method is suggested. For low inhomogeneity cases, the force method can predict the the mass flow with comparable accuracy to pressure measurements.

5.5 Paper E

CFD Investigation on Wheel Rotation Modelling

This work focused on the analysis of the MRFg method, previously introduced in Paper B. The analysis was first performed on an isolated wheel and compared to Sliding Mesh (SM) results. Then, the MRFg method was applied on special tyres mounted on a fully detailed production Volvo S60 and compared to experimental results.

The focus was on the rotation modelling of the tyre, hence the rim rotation modelling was only briefly investigated, as SM can be easily applied on a rigid circular geometry. In the isolated wheel simulations, it was shown that MRFg is able to reproduce similar flow field and ventilation moments to SM, on a detailed tyre. The Rotating Wall (RW) approach failed at that and could only reproduce the SM results on a slick tyre.

When comparing to experiments, MRFg showed great improvements to the drag prediction when lateral grooves are introduced on a tyre, compared to RW. It provided satisfactory results on two rim designs. The application of MRFg could be extended beyond tyre modelling and general guidelines are provided at the end of the paper.

5.6 Paper F

Tyre Pattern Features and their Effects on Passenger Vehicle Drag

This work investigated tyre pattern features in simulations and compared the results to measured drag changes on a full scale vehicle in the wind tunnel. For that purpose, special hand cut simplified tyres were used, in order to isolate the effects of the rain and lateral grooves. A detailed representation of the tyres was reproduced in the simulations and the MRFg method was utilized for modelling the lateral grooves.

First, some key parameters of the numerical methodology were investigated, namely the time step size and averaging time. Then, the various drag changes, from the different wheel configurations, were compared to the experimental results. The comparison showed good agreement on the open rim while the closed rim presented some deviations when the lateral grooves were present.

In simulations, the rain grooves showed an increase in base pressure and the lateral grooves locally increased the drag at the front wheel, without any further interactions downstream. It has also been seen, from the experimental results, that a detailed tyre could result in lower drag than a slick depending on the rim design.

References

[1] T. Hobeika, S. Sebben, and C. Landstrom. Investigation of the Influence of Tyre Geometry on the Aerodynamics of Passenger Cars. *SAE International Journal of Passenger Cars - Mechanical Systems* 6 (1 2013), pp. 316–325. ISSN: 1946-4002. DOI: 10.4271/2013-01-0955.

[2] T. Hobeika, S. Sebben, and L. Lofdahl. "Study of Different Tyre Simulation Methods and Effects on Passenger Car Aerodynamics". *International Vehicle Aerodynamics Conference 2014*. Holywell Park, Loughborough, UK, 2014, pp. 187–195. ISBN: 978-0-08-100199-8.

[3] T. Hobeika, S. Sebben, and L. Löfdahl. Experimental and numerical investigations of cooling drag. *Proceedings of the Institution of Mechanical Engineers, Part D: Journal of Automobile Engineering* 231.9 (2017), pp. 1203–1210. DOI: 10.1177/0954407016684740.

[4] T. Hobeika et al. Force Based Measurement Method for Cooling Flow Quantification. *SAE International Journal of Passenger Cars - Mechanical Systems* 10.2 (Mar. 2017), pp. 619–627. ISSN: 1946-4002. DOI: 10.4271/2017-01-1520.

[5] T. Hobeika and S. Sebben. CFD Investigation on Wheel Rotation Modelling. *Journal of Wind Engineering and Industrial Aerodynamics* 174 (2018), pp. 241–251. ISSN: 0167-6105.

[6] T. Hobeika and S. Sebben. "Tyre Pattern Features and their Effects on Passenger Vehicle Drag". *Accepted for publication in conjunction with SAE 2018 World Congress & Exhibition. Paper no: 2018-01-0710.*

[7] European Environment Agency. *National emissions reported to the UNFCCC and to the EU Greenhouse Gas Monitoring Mechanism.* http://www.eea.europa.eu/data-and-maps/data/national-emissions-reported-to-the-unfccc-and-to-the-eu-greenhouse-gas-monitoring-mechanism-13. 2017.

[8] Council of European Union. *Regulation (EC) 443/2009 of the European Parliament and of the Council setting emission performance standards for new passenger cars as part of the Community's integrated approach to reduce CO 2 emissions from*

light-duty vehicles.
http://data.europa.eu/eli/reg/2009/443/2013-05-08. 2013.

[9] Council of European Union. *Regulation (EU) No 333/2014 of the European Parliament and of the Council of 11 March 2014 amending Regulation (EC) No 443/2009 to define the modalities for reaching the 2020 target to reduce CO 2 emissions from new passenger cars*.
http://data.europa.eu/eli/reg/2014/333/oj. 2014.

[10] J. Fackarell and J. Harvey. "The Flow Field and Pressure Distribution of an Isolated Road Wheel". *Advances in Road Vehicle Aerodynamics*. Ed. by H. Stephens. Paper 10. Cranfield: BHRA Fluid Engineering, 1973, pp. 155–165.

[11] A. Cogotti. Aerodynamic characteristics of car wheels. *Int. Journal of Vehicle Design* (1983), pp. 173–196.

[12] L. Axon, K. Garry, and J. Howell. "An Evaluation of CFD for Modelling the Flow Around Stationary and Rotating Isolated Wheels". *International Congress & Exposition*. SAE International, Feb. 1998. DOI: 10.4271/980032. URL: https://doi.org/10.4271/980032.

[13] E. Mercker et al. "On the Aerodynamic Interference Due to the Rolling Wheels of Passenger Cars". *International Congress & Exposition*. SAE International, Feb. 1991. DOI: 10.4271/910311. URL: https://doi.org/10.4271/910311.

[14] E. Mercker and H. Berneburg. "On the Simulation of Road Driving of a Passenger Car in a Wind Tunnel Using a Moving Belt and Rotating Wheels". *3rd Int. Conf. Innovation and Reliability*. Florence, April 8-10, 1992.

[15] E. Mercker, H. Soja, and J. Wiedeman. "Experimental investigation on the influence of various ground simulation techniques on a passenger car". *Vehicle Aerodynamics*. Royal Aeronautical Society, July 1994.

[16] M. Pfadenhauer, G. Wickern, and K. Zwicker. "On the Influence of Wheels and Tyres on the Aerodynamic Drag of Vehicles". *MIRA International Conference on Vehicle Aerodynamics*. 1996.

[17] G. Wickern. "The Effect of Moving Ground on the Aerodynamic Drag of a Production Car". *SATA Conference*. 1991.

[18] G. Wickern, K. Zwicker, and M. Pfadenhauer. *Rotating Wheels - Their Impact on Wind Tunnel Test Techniques and on Vehicle Drag Results*. Paper No: 970133. Warrendale and PA: SAE International, 1997.

[19] A. P. Mears, R. G. Dominy, and D. B. Sims-Williams. "The Air Flow About an Exposed Racing Wheel". *Motorsports Engineering Conference & Exhibition*. SAE International, Dec. 2002. DOI: 10.4271/2002-01-3290. URL: https://doi.org/10.4271/2002-01-3290.

[20] I. Dimitriou and S. Klussmann. "Aerodynamic Forces of Exposed and Enclosed Rotating Wheels as an Example of the Synergy in the Development of Racing and Passenger Cars". *SAE 2006 World Congress & Exhibition*. SAE International, Apr. 2006. DOI: 10.4271/2006-01-0805. URL: https://doi.org/10.4271/2006-01-0805.

[21] P. Elofsson and M. Bannister. "Drag Reduction Mechanisms Due to Moving Ground and Wheel Rotation in Passenger Cars". *SAE 2002 World Congress & Exhibition*.

SAE International, Mar. 2002. DOI: 10.4271/2002-01-0531. URL: https://doi.org/10.4271/2002-01-0531.

[22] C. Landström, L. Löfdahl, and T. Walker. *Detailed Flow Studies in Close Proximity of Rotating Wheels on a Passenger Car*. Paper No: 2009-01-0778. Warrendale and PA: SAE International, 2009.

[23] C. Landström et al. "An experimental investigation of wheel design parameters with respect to aerodynamic drag". *8th FKFS Conference-Progress in Vehicle Aerodynamics and Thermal Management*. Stuttgart, 2011.

[24] C. Landström et al. *Influences of Different Front and Rear Wheel Designs on Aerodynamic Drag of a Sedan Type Passenger Car*. Paper No: 2011-01-0165. Warrendale and PA: SAE International, 2011.

[25] W. Mayer and J. Wiedemann. "The Influence of Rotating Wheels on Total Road Load". *SAE World Congress & Exhibition*. SAE International, Apr. 2007. DOI: 10.4271/2007-01-1047. URL: https://doi.org/10.4271/2007-01-1047.

[26] J. McManus and X. Zhang. A Computational Study of the Flow Around an Isolated Wheel in Contact With the Ground. *Journal of Fluids Engineering* 128.3 (2006), p. 520. ISSN: 00982202.

[27] F. Modlinger, R. Demuth, and N. Adams. "New Directions in the Optimization of the Flow around Wheels and Wheel Arches". *MIRA International Conference on Vehicle Aerodynamics*. 2008.

[28] A. F. Skea, P. R. Bullen, and J. Qiao. "CFD Simulations and Experimental Measurements of the Flow Over a Rotating Wheel in a Wheel Arch". *SAE 2000 World Congress*. SAE International, Mar. 2000. DOI: 10.4271/2000-01-0487. URL: https://doi.org/10.4271/2000-01-0487.

[29] A. Wäschle et al. "Flow around an Isolated Wheel - Experimental and Numerical Comparison of Two CFD Codes". *SAE 2004 World Congress & Exhibition*. SAE International, Mar. 2004. DOI: 10.4271/2004-01-0445. URL: https://doi.org/10.4271/2004-01-0445.

[30] A. Wäschle. *The Influence of Rotating Wheels on Vehicle Aerodynamics - Numerical and Experimental Investigations*. Paper No: 2004-01-0445. Warrendale and PA: SAE International, 2007. DOI: \url{10.4271/2007-01-0107}.

[31] S. Koitrand, A. Gaylard, and G. O. Fiet. "An Investigation of Wheel Aerodynamic Effects for a Saloon Car". *Progress in Vehicle Aerodynamics and Thermal Management: Proceedings of the 10th FKFS-Conference*. Reihe Technik. 2015. ISBN: 9783816933229. URL: https://books.google.se/books?id=GynYjgEACAAJ.

[32] L. Haag, T. Blacha, and T. Indinger. Experimental Investigation on the Aerodynamics of Isolated Rotating Wheels and Evaluation of Wheel Rotation Models Using Unsteady CFD. *International Journal of Automotive Engineering* 8.1 (2017), pp. 7–14. DOI: 10.20485/jsaeijae.8.1_7.

[33] A. D'Hooge et al. "The Aerodynamic Development of the Tesla Model S - Part 2: Wheel Design Optimization". *SAE 2012 World Congress & Exhibition*. SAE International, Apr. 2012. DOI: 10.4271/2012-01-0178. URL: https://doi.org/10.4271/2012-01-0178.

[34] P. Mlinaric. "Investigations of the Influence of Tyre Deformation and Tyre Contact Patch on CFD Predictions of Aerodynamic Forces on a Passenger Car". Master's Thesis. Gothenburg: Chalmers University of Technology, 2007.

[35] F. Wittmeier et al. "Model Scale Based Process for the Development of Aerodynamic Tire Characteristics". *SAE Technical Paper*. SAE International, Apr. 2014. DOI: 10.4271/2014-01-0585.

[36] B. Schnepf, T. Schütz, and T. Indinger. Further Investigations on the Flow Around a Rotating, Isolated Wheel with Detailed Tread Pattern. *SAE Int. J. Passeng. Cars - Mech. Syst.* 8 (Apr. 2015), pp. 261–274. DOI: 10.4271/2015-01-1554.

[37] C. Landstrom et al. Aerodynamic Effects of Different Tire Models on a Sedan Type Passenger Car. *SAE Int. J. Passeng. Cars - Mech. Syst.* 5 (Apr. 2012), pp. 136–151. DOI: 10.4271/2012-01-0169.

[38] F. Wittemeier et al. "Classification of Aerodynamic Tyre Characteristics". *International Vehicle Aerodynamics Conference 2014*. Holywell Park, Loughborough, UK, 2014, pp. 175–185. ISBN: 978-0-08-100199-8.

[39] B. Schnepf, G. Tesch, and T. Indinger. "Investigations on the Flow around Wheels using Different Road Simulation Tools". *Progress in Vehicle Aerodynamics and Thermal Management*. Stuttgart, Germany, 2013, pp. 155–166. ISBN: 978-3-8169-3253-6.

[40] S. Diasinos, T. J. Barber, and G. Doig. The effects of simplifications on isolated wheel aerodynamics. *Journal of Wind Engineering and Industrial Aerodynamics* 146 (2015), pp. 90–101. ISSN: 0167-6105. DOI: 10.1016/j.jweia.2015.08.004. URL: http://www.sciencedirect.com/science/article/pii/S0167610515001968.

[41] P. Mlinaric and S. Sebben. "Investigation of the Influence of Tyre Deflection and Tyre Contact Patch on CFD Predictions of Aerodynamic Forces on a Passenger Car". *MIRA International Conference on Vehicle Aerodynamics*. 2008.

[42] A. J. Sprot, D. B. Sims-Williams, and R. G. Dominy. The Aerodynamic Characteristics of a Fully Deformable Formula One Wind Tunnel Tyre. *SAE Int. J. Passeng. Cars - Mech. Syst.* 5.2 (Apr. 2012), pp. 1026–1041. ISSN: 1946-4002. DOI: 10.4271/2012-01-1166. URL: https://doi.org/10.4271/2012-01-1166.

[43] C. Lew et al. "Aerodynamic Simulation of a Standalone Rotating Treaded Tire". *WCX17: SAE World Congress Experience*. SAE International, Apr. 2017. DOI: 10.4271/2017-01-1551. URL: https://doi.org/10.4271/2017-01-1551.

[44] S. Chaligne, R. Turner, and A. Gaylard. "The aerodynamics development of the New Land Rover Discovery". *11th FKFS Conference-Progress in Vehicle Aerodynamics and Thermal Management*. Stuttgart, 2017.

[45] S. Kandasamy et al. "Aerodynamic Performance Assessment of BMW Validation Models using Computational Fluid Dynamics". *SAE 2012 World Congress & Exhibition*. SAE International, Apr. 2012. DOI: 10.4271/2012-01-0297. URL: https://doi.org/10.4271/2012-01-0297.

[46] J. Sterneus, T. Walker, and T. Bender. "Upgrade of the Volvo Cars Aerodynamic Wind Tunnel". *SAE Technical Paper*. Detroit, Michigan: SAE International, 2007. DOI: 10.4271/2007-01-1043.

[47] M. L. Shur et al. A hybrid RANS-LES approach with delayed-DES and wall-modelled LES capabilities. *International Journal of Heat and Fluid Flow* 29.6 (2008), pp. 1638–

1649. ISSN: 0142-727X. DOI: 10.1016/j.ijheatfluidflow.2008.07.001. URL: http://www.sciencedirect.com/science/article/pii/S0142727X08001203.

[48] J. C. Hunt, A. Wray, and P. Moin. Eddies, stream, and convergence zones in turbulent flows. *Center for turbulence research report CTR-S88* (1988), pp. 193–208.

[49] W. H. Hucho. *Aerodynamics of Road Vehicles*. Fourth. Warrendale, USA: Society of Automotive Engineers, Inc, 1998, pp. 559–561. ISBN: 0-7680-0029-7.

[50] G. Tesch, R. Demuth, and N. Adams. A New Approach to Analyzing Cooling and Interference Drag. *SAE Int. J. Passeng. Cars – Mech. Syst.* 3 (Apr. 2010), pp. 339–351. DOI: 10.4271/2010-01-0286. URL: http://dx.doi.org/10.4271/2010-01-0286.

[51] J. Williams. "Aerodynamic Drag of Engine-Cooling Airflow With External Interference". *SAE Technical Paper*. SAE International, Mar. 2003. DOI: 10.4271/2003-01-0996. URL: http://dx.doi.org/10.4271/2003-01-0996.

[52] T. Wolf. "Minimising the Cooling System Drag for the New Porsche 911 Carrera". *5th MIRA International Vehicle Aerodynamics Conference, 13-14 October 2004, Warwick, UK*. Warwick, UK: MIRA, Oct. 2004.

[53] H. Soja and J. Wiedemann. The interference between exterior and interior flow on road vehicles. *Journee d'etude: Dynamique du vehicule – Securite Active* (Sept. 1987), pp. 101–105.

[54] E. Y. Ng et al. "Use of Pressure-Based Technique for Evaluating the Aerodynamics of Vehicle Cooling Systems". *SAE Technical Paper*. Detroit, Michigan: SAE International, 2002. DOI: 10.4271/2002-01-0712.

[55] R. Ruijsink. "The Use of the MicroProbe System in Cooling System Development". *Third MIRA International Vehicle Aerodynamics Conference*. Rugby, UK, 2000. ISBN: 0952415623.

[56] S. Wille et al. Integrated Numerical and Experimental Approach to Determine the Cooling Air Mass Flow in Different Vehicle Development Stages. *SAE Int. J. Passeng. Cars - Mech. Syst.* 3 (1 2010), pp. 352–365. ISSN: 1946-4002. DOI: 10.4271/2010-01-0287.

[57] J. F. Foss et al. The Thermal Transient Anemometer. *Measurement Science and Technology* 15 (11 2004), pp. 2248–2255. DOI: 10.1088/0957-0233/15/11/010.

[58] J. Williams. "An Automotive Front-End Design Approach for Improved Aerodynamics and Cooling". *SAE Technical Paper*. Detroit, Michigan: SAE International, 1985. DOI: 10.4271/850281.

[59] J. Williams and G. Vemaganti. "CFD Quality - A Calibration Study for Front-End Cooling Airflow". *SAE Technical Paper*. Detroit, Michigan: SAE International, 1998. DOI: 10.4271/980039.

[60] P. V. Gullberg. "Optimisation of the Flow Process in Engine Bays- 3D Modelling of Cooling Airflow". PhD thesis. Gothenburg, Sweden, 2011, pp. 239–245. ISBN: 978-91-7385-559-4.

[61] M. Eng. "Investigation of Aerodynamic correction methods applied to a slotted wall Wind Tunnel". Master's Thesis. Berlin, Germany: TU Berlin, 2009.